Front. Mech. Eng. 2023, 18(3): 40
https://doi.org/10.1007/s11465-023-0756-0

RESEARCH ARTICLE

Comprehensive kinetostatic modeling and morphology characterization of cable-driven continuum robots for *in-situ* aero-engine maintenance

Zheshuai YANG, Laihao YANG (✉), Yu SUN, Xuefeng CHEN

School of Mechanical Engineering, Xi'an Jiaotong University, Xi'an 710049, China

✉ *Corresponding author. E-mail: yanglaihao@xjtu.edu.cn (Laihao YANG)*

ABSTRACT *In-situ* maintenance is of great significance for improving the efficiency and ensuring the safety of aero-engines. The cable-driven continuum robot (CDCR) with twin-pivot compliant mechanisms, which is enabled with flexible deformation capability and confined space accessibility, has emerged as a novel tool that aims to promote the development of intelligence and efficiency for *in-situ* aero-engine maintenance. The high-fidelity model that describes the kinematic and morphology of CDCR lays the foundation for the accurate operation and control for *in-situ* maintenance. However, this model was not well addressed in previous literature. In this study, a general kinetostatic modeling and morphology characterization methodology that comprehensively contains the effects of cable-hole friction, gravity, and payloads is proposed for the CDCR with twin-pivot compliant mechanisms. First, a novel cable-hole friction model with the variable friction coefficient and adaptive friction direction criterion is proposed through structure optimization and kinematic parameter analysis. Second, the cable-hole friction, all-component gravities, deflection-induced center-of-gravity shift of compliant joints, and payloads are all considered to deduce a comprehensive kinetostatic model enabled with the capacity of accurate morphology characterization for CDCR. Finally, a compact continuum robot system is integrated to experimentally validate the proposed kinetostatic model and the concept of *in-situ* aero-engine maintenance. Results indicate that the proposed model precisely predicts the morphology of CDCR and outperforms conventional models. The compact continuum robot system could be considered a novel solution to perform *in-situ* maintenance tasks of aero-engines in an invasive manner.

KEYWORDS kinetostatic modeling, morphology characterization, variable friction, continuum robots, *in-situ* maintenance

1 Introduction

In-situ aero-engine maintenance works, i.e., inspection and repair, are highly beneficial because they can significantly reduce the currently accepted maintenance cycle, which is extensive and costly due to the requirement to disassemble engines from the wing of an aircraft [1,2]. However, the lack of highly flexible and slender (i.e., sizeable length-to-diameter ratio) specialized inspection/repair tools has always impeded the goal of achieving highly efficient and intelligent *in-situ* maintenance for aero-engines. Recent advances in the field of intelligent robotics have resulted in cable-driven continuum robots (CDCRs) that have excellent flexibility and improved accessibility in unstructured and highly restricted spaces, showing unique strengths and potential for *in-situ* aero-engine maintenance [3–5].

However, the unstructured and highly restricted space in aero-engines require the design and control of CDCRs to enable more dexterous obstacle avoidance and a larger length-to-diameter ratio rather than a mere increase in the length or a reduced radial size. The conventional CDCRs, which are mainly based on a central backbone, suffer from the torsion problem under the effects of gravity and payloads, leading to significant difficulty in achieving high position accuracy. The CDCR with twin-pivot compliant mechanisms was previously proposed in Refs. [2,6] to address this issue and has been proven to achieve excellent torsion resistance [7,8]. However, the high-fidelity model that characterizes the kinetostatic and morphology of CDCR and further lays the foundation for

Received December 9, 2022; accepted April 27, 2023

the accurate operation and control for *in-situ* maintenance has not been well addressed in their study; this subject is the first-line issue on which this paper focuses.

The CDCR has the advantages of flexibility and dexterity. However, it poses significant challenges for accurate mathematical modeling of the kinetostatic and morphology because of compliant and hyper-redundant mechanisms. The kinematic model of rigid-link robots can be directly deduced by using the Denavit–Hartenberg (D–H) method. However, the D–H method cannot be directly applied to the kinematic modeling of CDCR. Therefore, some necessary assumptions are generally employed to establish the kinematic model of CDCR due to the compliant mechanism adopted. The widely applied assumption is constant curvature theory [6,8–14], as shown in Fig. 1(a), which assumes each section as a constant arc, thus simplifying the kinematics significantly. However, the classical constant curvature-based kinematics model often suffers from defects, such as model mismatch under the large deflection of compliant mechanism and the ignorance of the effects of mechanical properties such as loads, gravity, and friction. As a result, significant errors occur with the increase in the length-to-diameter ratio of CDCRs [15,16].

Given such situation, improving kinematics model accuracy has been one of the focuses in the field of continuum robotics in recent years. The variable curvature-based kinematic modeling method, which adopts various geometrical techniques (such as mode shape function methods [17], Bezier curve method [18], Euler spiral methods [19], and Pythagorean-hodograph curve methods [20,21]) to approximate the deflection of compliant mechanism [22], is believed to be able to characterize the morphology of CDCRs better and more precisely. However, this approach is often employed to formulate the kinematic model of soft continuum robots, such as pneumatic-driven continuum robots, where the cable-hole property of CDCRs does not need to be considered. Moreover, for the soft continuum robots, the morphology of the whole section can be estimated through geometrical techniques because no segmented discs exist. Thus, it can be modeled as continuous backbones. However, this modeling methodology may also lead to model mismatch and further tip position errors for the CDCR with segmented discs (central backbones) [23] and, even seriously, fails for the CDCR with a twin-pivot compliant mechanism because of the varying deflection of any adjacent flexible backbones in each section.

Currently, a robust way to address this issue is to model each compliant backbone individually by using methods such as the finite element method (FEM) [24,25] and the piecewise constant curvature (PCC) method illustrated in Fig. 1(b). The FEM-based kinematic models accurately characterize the deflection of flexible backbones and including mechanical factors [14]. However, FEM usually needs a large amount of computation, hence being time consuming, which is adverse to real-time modeling and control of CDCR [26]. The PCC-based kinematic model is developed from the constant curvature method and assumes each compliant backbone rather than each section as a constant arc [15], thus making it possible to separately model the adjacent compliant backbone and further precisely characterizing the morphology of the CDCR. However, the classical PCC-based kinematic model mainly focuses on the geometrical description of the CDCR, where the mapping between actuation system space and the configuration space under the influence of mechanical factors such as the payloads, gravity, and friction are generally ignored.

The static model, another widely discussed methodology for the kinematic modeling of the CDCR, often employs Cosserat-rod theory [27–29], Kirchhoff elastic rod theory [1,30], and beam constraint model [31–33] to characterize the deformation of compliant mechanisms. Thus, it can consider mechanical properties such as payload, gravity, and friction [15,34]. However, conventional static models are generally developed for

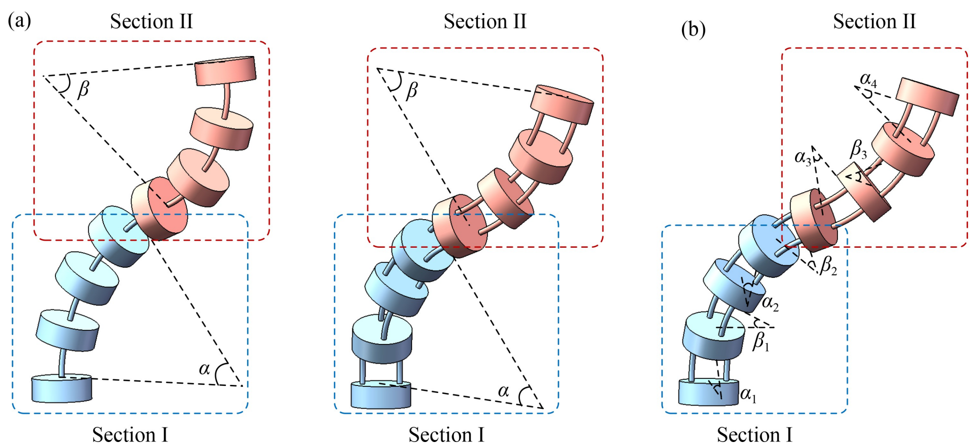

Fig. 1 Assumptions of kinematics: (a) constant curvature assumption and (b) piecewise constant curvature assumption.

central backbone continuum robots and adopt the constant friction model. Chen et al. [16] further investigated the kinematics model of multi-backbone continuum robots on the basis of variable curvature assumption and Cosserat-rod theory, focusing on the mechanical factors of elastic elongation of backbones and external payloads. The above investigations significantly promote the development of kinematic modeling of continuum robots and prove that the static model outperforms the pure kinematic model in terms of modeling accuracy and morphology characterization for central backbone continuum robots.

However, the state-of-the-art static models may fail to characterize the actual morphology of CDCR with twin-pivot compliant mechanisms. Unlike the central backbone structure, the two adjacent vertical-cross bending joints of the twin-pivot compliant mechanism inherently have different deflections, resulting in various mechanical properties. Furthermore, the model mismatch caused by the constant curvature assumption indicates that each segment (i.e., twin-pivot compliant mechanism) of the section should not be regarded evenly. Thus, their mechanical parameters should not be identical, which was neglected in previous works [15,35,36]. For example, most static models assume the friction coefficient as a constant value, which may fail to accurately describe the morphology when the CDCR is under different deflections. Although some frictionless models demonstrated that friction is negligible when the CDCR is under the small deflection approximation because the friction generated by radial pressure is slight under this condition, it is not applicable to the case under the large deformation condition [29,35]. According to the theoretical and experimental analysis, the cable-hole friction coefficient should be a function of bending angles rather than a constant value [1,15], which will be deduced in detail in the text. Furthermore, the friction direction of the same driving cable may differ at different joints, indicating a need for separately determined friction direction criterion.

Another influencing factor that is often neglected is the gravities of all components, including discs, cables, cable-locking devices on CDCR, compliant backbones, and deflection-induced center-of-gravity shift of compliant joints. In conventional models, only the gravities of discs are considered, and the gravities of other components are believed to be slighter than the entire CDCR, thereby further contributing to the low position accuracy. With the urgent need for a large length-to-diameter ratio and the development of a lightweight design for CDCRs, the gravities of the components of compliant backbones, cables, and cable-locking devices have been increased to a comparable level to the components of discs, which indicates that they should no longer be neglected. For example, the gravities of the testing prototype of CDCR in this study account for more than 30% of the entire CDCR. This proportion depends on the section number and length-to-diameter ratio of the CDCR. Therefore, the gravities of all components should be involved in the kinetostatic modeling of the CDCR.

This paper aims to address the above issues for the CDCR with the twin-pivot compliant mechanism. The main contributions are as follows:

1) A general kinetostatic model enabled with accurate kinematic modeling and morphology characterization of CDCR with twin-pivot compliant mechanisms is developed by comprehensively considering the effects of cable-hole friction, gravity, and payloads. The proposed kinetostatic modeling methodology can be easily extended and applied to other kinds of CDCRs.

2) A novel cable-hole friction model with the variable friction coefficient and adaptive friction direction criterion is proposed through structure optimization and kinematic parameter analysis.

3) The effects of all-component gravities, the deflection-induced center-of-gravity shift of compliant joints, and payloads are all considered for the first time to deduce the comprehensive kinetostatic model.

The remainder of this paper is organized as follows: The continuum robot system is constructed and optimized in Section 2; the kinematic model is established in Section 3; a comprehensive kinetostatic model is proposed based on the analysis of compliant mechanisms, kinematics, and statics in Section 4; the variable friction coefficient is identified in Section 5; experimental validation is performed in Section 6; the whole paper is summarized and the conclusion is presented in the last section.

2 Continuum robot design and optimization

The CDCR in this study (Fig. 2) is developed based on the prototype, i.e., the twin-pivot CDCR, proposed by Mohammad et al. [37]. The weight of the whole manipulator was reduced and the cable-hole friction modeling was simplified by using the lightweight design and special joint disc design to optimize the CDCR, thus enabling us to develop a novel friction model with a variable coefficient. The structure overview, optimization, and control system will be briefly introduced in this section.

2.1 Overview of the continuum robot system

The continuum robot system is illustrated in Fig. 3. Each section comprises several identical segments and is driven by four cables. As shown in Fig. 3(c), each segment consists of three optimized discs connected by twin-pivot backbones, i.e., Ni–Ti rods. The disc is approximately ring shaped with a diameter of 16 mm and a thickness of 6 mm, which allows the continuum manipulator to access

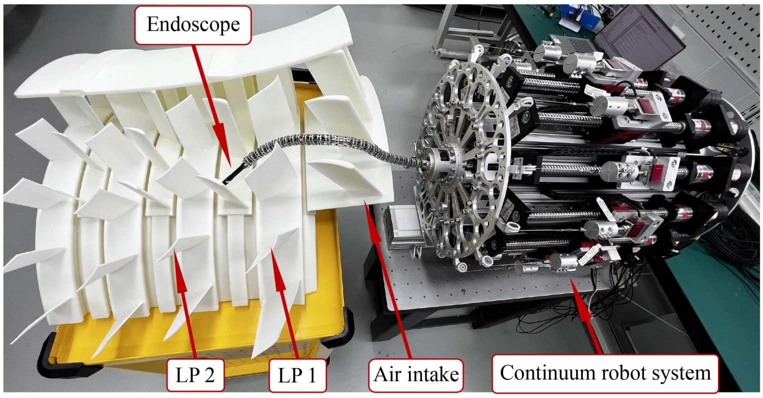

Fig. 2 Continuum robot for *in-situ* inspection of aero-engine.

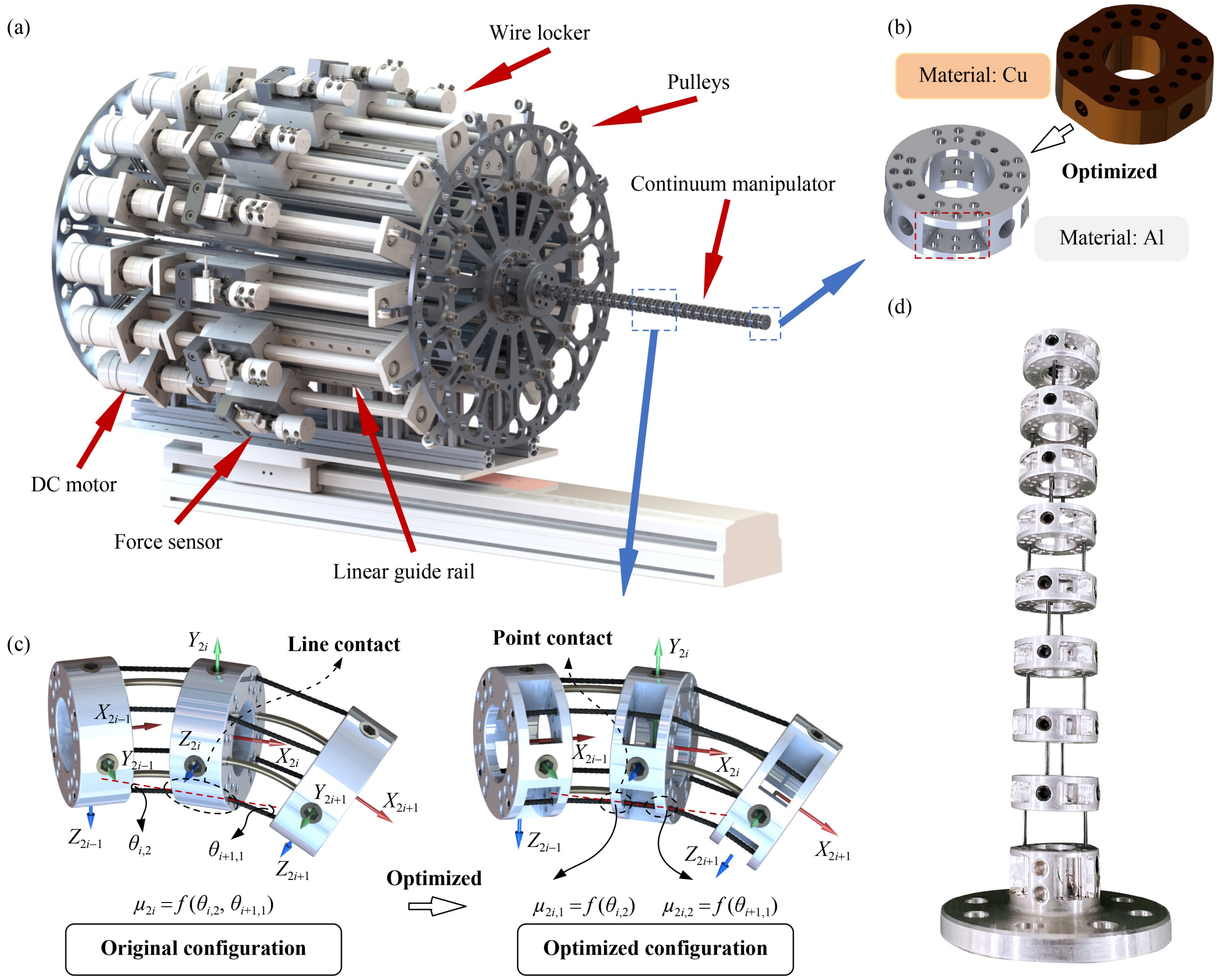

Fig. 3 Continuum robot system: (a) overview of the optimized continuum robot system, (b) optimization of the disc, (c) optimization of contact friction, and (d) single-section prototype of the optimized continuum manipulator.

the aero-engine and perform *in-situ* damage inspection or repair. The diameter of the Ni–Ti rod is 0.8 mm. The performance index is listed in Table 1.

2.2 Optimization of the compliant twin-pivot mechanism

The twin-pivot compliant mechanism was reported in previous work [13]. In this subsection, two steps are adopted to optimize the structure of the compliant mechanism and reduce the weight of the entire robot. 1) The contact area between the driving cable and the disc hole is redesigned to avoid the uncertain line contact in the original structure, as illustrated in Fig. 3(c). The optimized design significantly reduces the contact area,

Table 1 Parameters of the CDCR

Parameter	Values
Length-to-diameter ratio	22.5
Entire length of the continuum manipulator	360 mm
Degree of freedom (DOF)	6 + 1
Disc number (single section)	10
Motor number	12 + 1
Bending capability (single section/entire CDCR)	−72° to +72°; −216° to +216°
Disc diameter	16 mm
Disc mass	1.4 g

thus reducing the friction effect. As a result, the cable-hole contact of the optimized structure can be simplified to point contact because the disc is so thin. Moreover, the optimized design made it possible to model the cable-hole friction behavior separately on two sides of the disc, which may result in different cable-hole friction behavior because the compliant mechanism of different sides deforms in different directions and with different deflections. 2) Two techniques, as illustrated in Fig. 3(b), are adopted to realize the lightweight design: The hollow-carved disc structure inherently reduces weight compared with the original structure, and light material is employed to fabricate the disc.

The simplified friction modeling process is analyzed in detail in this section and will be mathematically deduced in the modeling section. The primary motivation for this optimization design comes from our previous theoretical considerations and experimental observations. According to the theory of contact mechanics, the friction force is greatly affected by the contact area. However, for the original disc configuration, the real-time line contact area is hard to evaluate because the compliant mechanism on two sides of the disc deforms in different directions and with different deflections. Moreover, the friction force of the original disc configuration depends on the compliant mechanisms' bending angles on both sides, as shown in Fig. 3(c), which may further complicate the friction model because the two angles are in two vertical planar workspaces. Considering this situation, the original disc structure is optimized to divide the one line contact into two point contacts between driving cables and disc holes, as shown in Fig. 3(b). This small structure optimization step provides the following benefits: The contact area and the uncertainty during friction modeling are reduced significantly, and the possibility of separately constructing the friction model depending only on one joint angle at each side is increased, thus avoiding the complication of formulating the friction model as a function of two angles.

2.3 Actuation and control system design

As illustrated in Fig. 3, the actuation system mainly consists of direct current (DC) motors (M3508 P19), linear guide rails, wire lockers, and pulleys. The force sensors are integrated into the actuation system, which is employed to detect the cable tension. The DC motors are driven by electronic speed controllers (ESCs) and connected by a controller area network bus. The motion of the continuum robot is controlled by the STM32F407 through the cable length variations that are calculated on the personal computer (PC) and sent to the STM32 via serial communication. The pulleys are employed to change the direction of cables. As a result, the actuation and control system drives the continuum manipulator by transmitting the actuating force through the driving cables.

3 Kinematic modeling

The kinematics of the CDCR is established based on the PCC assumption, which lays the foundation of the kinetostatic analysis. Unlike in our previous work [6,13], each compliant backbone rather than each section is assumed as an independent curvature in this paper, as illustrated in Fig. 1.

As illustrated in Fig. 4, the transformation matrix from $\{O_{2i-2}\}$ to $\{O_{2i-1}\}$ can be expressed as

$$ {}^{2i-2}_{2i-1}\boldsymbol{T} = \textbf{Trans}\left(\frac{L}{\beta_{i,1}}\tan\frac{\beta_{i,1}}{2}+\frac{h}{2},0,0\right)\cdot\textbf{Rot}(z_{2i-1},\beta_{i,1}) \cdot\textbf{Rot}\left(x_{2i-1},\frac{\pi}{2}\right)\cdot\textbf{Trans}\left(\frac{L}{\beta_{i,1}}\tan\frac{\beta_{i,1}}{2}+\frac{h}{2},0,0\right), \quad (1)$$

where $\{o_{2i}\}$: $o-x_{2i}y_{2i}z_{2i}$ is the $2i$th revolute joint frame, $\{O_{\rm G}\}$: $O-X_{\rm G}Y_{\rm G}Z_{\rm G}$ is the ith disc frame with the origin O_{2i} at the center of the ith disc, ${}^{i}_{i+1}T$ is the transformation matrix from frame $\{O_i\}$ to frame $\{O_{i+1}\}$, L is the length of Ni–Ti rod, $\beta_{i,1}$ is the first joint angle of the ith segment, h is the thickness of the disc, $\textbf{Rot}(x_i,\alpha)$ is the rotation transformation matrix of the rotation α angle about the x_i axis, $\textbf{Trans}(x,y,z)$ is the translation transformation matrix of the vector $[x,y,z]$, and the transformation matrix from $\{O_{2i-1}\}$ to $\{O_{2i}\}$ can be expressed as

$$ {}^{2i-1}_{2i}\boldsymbol{T} = \textbf{Trans}\left(\frac{L}{\beta_{i,2}}\tan\frac{\beta_{i,2}}{2}+\frac{h}{2},0,0\right)\cdot\textbf{Rot}(z_{2i},\beta_{i,2}) \cdot\textbf{Rot}\left(x_{2i},-\frac{\pi}{2}\right)\cdot\textbf{Trans}\left(\frac{L}{\beta_{i,2}}\tan\frac{\beta_{i,2}}{2}+\frac{h}{2},0,0\right), \quad (2)$$

where $\beta_{i,2}$ is the second joint angle of the ith segment. Thus, the kinematics of the ith segment can be written as

$$ {}^{2i-2}_{2i}\boldsymbol{T} = {}^{2i-2}_{2i-1}\boldsymbol{T}\cdot{}^{2i-1}_{2i}\boldsymbol{T}, \quad (3)$$

and the jth cable length variation in $(2i-1)$th plane and $2i$th plane can be given by

$$\begin{cases} \Delta l_{\mathrm{D}_{2i-1}\mathrm{C}_j} = 2\left(\dfrac{L}{\beta_{i,1}} - r_j\cos\phi_j\right)\sin\dfrac{\beta_{i,1}}{2} - L, \\ \Delta l_{\mathrm{D}_{2i}\mathrm{C}_j} = 2\left(\dfrac{L}{\beta_{i,2}} - r_j\sin\phi_j\right)\sin\dfrac{\beta_{i,2}}{2} - L, \end{cases} \quad (4)$$

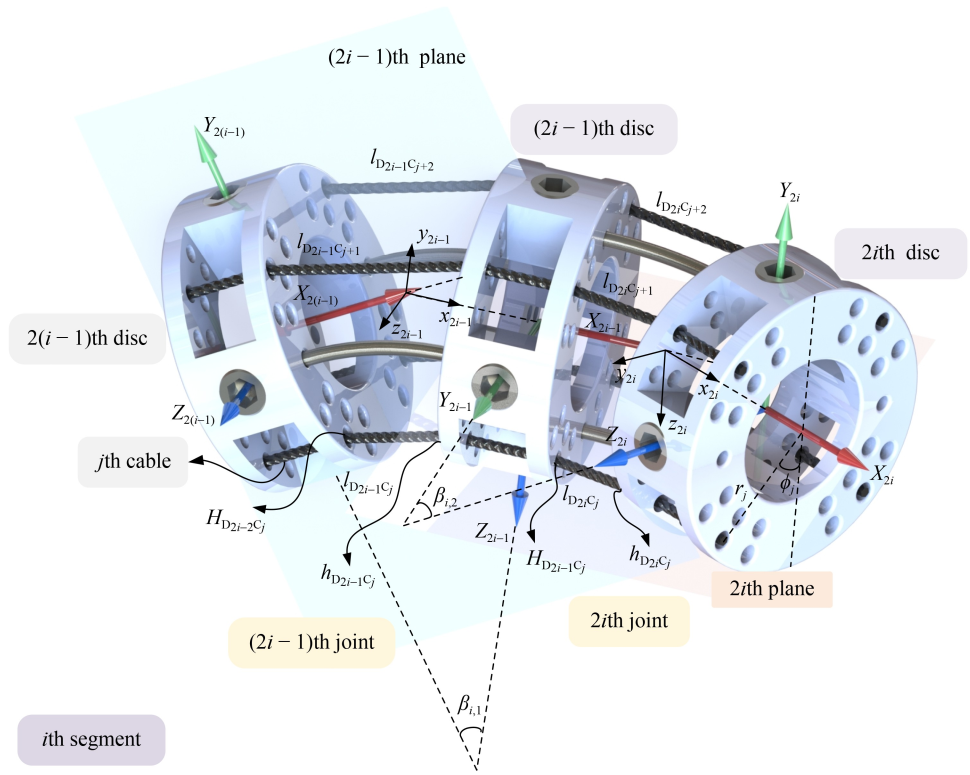

Fig. 4 Kinematics of one segment.

where $\Delta l_{\mathrm{D}_{2i-1}\mathrm{C}_j}$ and $\Delta l_{\mathrm{D}_{2i}\mathrm{C}_j}$ are the jth cable variations of the $(2i-1)$th and $2i$th joints in the ith segment, r_j is the distance of the jth cable hole and the disc center, and ϕ_j is the angle of the jth cable hole and Y_i axis. Hence, the kinematics of the continuum robot can be obtained by Eqs. (1)–(4).

4 Kinetostatic modeling

In this section, a comprehensive kinetostatic model is proposed to characterize the morphology of the CDCR on the basis of a theoretical analysis of the kinematics and mechanical properties of CDCR. The mechanical properties considered in this study are classified into four categories: 1) the actuating and friction forces generated by driving cables and cable-hole contact, respectively; 2) the gravities of all components, including discs, compliant backbones, cables, and cable-locking devices; 3) the elasticity of compliant backbones; and 4) the external forces and moments. The modeling of these mechanical properties will be mathematically deduced based on the following necessary assumptions:

1) Each compliant twin-pivot mechanism is considered a planar super-elastic rod that is inextensible and untwisted [1], implying that the two bending joints of each segment are constrained to two vertical planar workspaces.

2) Each compliant backbone is assumed as a constant curvature, and the extension deformations of driving cables caused by tension are neglected.

4.1 Actuating force modeling

As illustrated in Fig. 3, the CDCR is chained by several identical segments. Thus, the kinetostatics of the whole continuum robot can be formulated by investigating the kinetostatic behavior of one segment. The schematic of two segments is shown in Fig. 5. The actuating force of the jth cable to the $2i$th disc, which is expressed in the frame $\{O_{2i-1}\}$, can be described as

$$\begin{aligned}\boldsymbol{F}_{\mathrm{D}_{2i}\mathrm{C}_j}^{O_{2i-1}} &= \boldsymbol{F}_{\mathrm{J}_{2i}\mathrm{C}_j}^{O_{2i-1}} + \boldsymbol{F}_{\mathrm{J}_{2i+1}\mathrm{C}_j}^{O_{2i-1}} \\ &= F_{\mathrm{J}_{2i}\mathrm{C}_j} \cdot \frac{H_{\mathrm{D}_{2i-1}\mathrm{C}_j}^{O_{2i-1}} - h_{\mathrm{D}_{2i}\mathrm{C}_j}^{O_{2i-1}}}{\left\| H_{\mathrm{D}_{2i-1}\mathrm{C}_j}^{O_{2i-1}} - h_{\mathrm{D}_{2i}\mathrm{C}_j}^{O_{2i-1}} \right\|} + F_{\mathrm{J}_{2i+1}\mathrm{C}_j} \cdot \frac{h_{\mathrm{D}_{2i+1}\mathrm{C}_j}^{O_{2i-1}} - H_{\mathrm{D}_{2i}\mathrm{C}_j}^{O_{2i-1}}}{\left\| h_{\mathrm{D}_{2i+1}\mathrm{C}_j}^{O_{2i-1}} - H_{\mathrm{D}_{2i}\mathrm{C}_j}^{O_{2i-1}} \right\|},\end{aligned} \tag{5}$$

where $\boldsymbol{F}_{\mathrm{D}_i\mathrm{C}_j}^{O_{i-1}}$ is the actuating force vector applied by the jth cable to the ith disc expressed in frame $\{O_{i-1}\}$, $\boldsymbol{F}_{\mathrm{J}_{2i}\mathrm{C}_j}^{O_{2i-1}}$ and $\boldsymbol{F}_{\mathrm{J}_{2i+1}\mathrm{C}_j}^{O_{2i-1}}$ are the jth cable tensions in the $2i$th and $(2i+1)$th joint, respectively, which is expressed in the frame $\{O_{2i-1}\}$, $F_{\mathrm{J}_i\mathrm{C}_j}$ is the value of jth cable tension in the ith joint, $H_{\mathrm{D}_{2i}\mathrm{C}_j}^{O_{2i-1}}$ and $h_{\mathrm{D}_{2i}\mathrm{C}_j}^{O_{2i-1}}$ are the jth cable holes on the $2i$th disc. Similarly, the actuating force of another side cable (opposite to the jth cable, i.e., the $(j+2)$th cable) can be expressed as

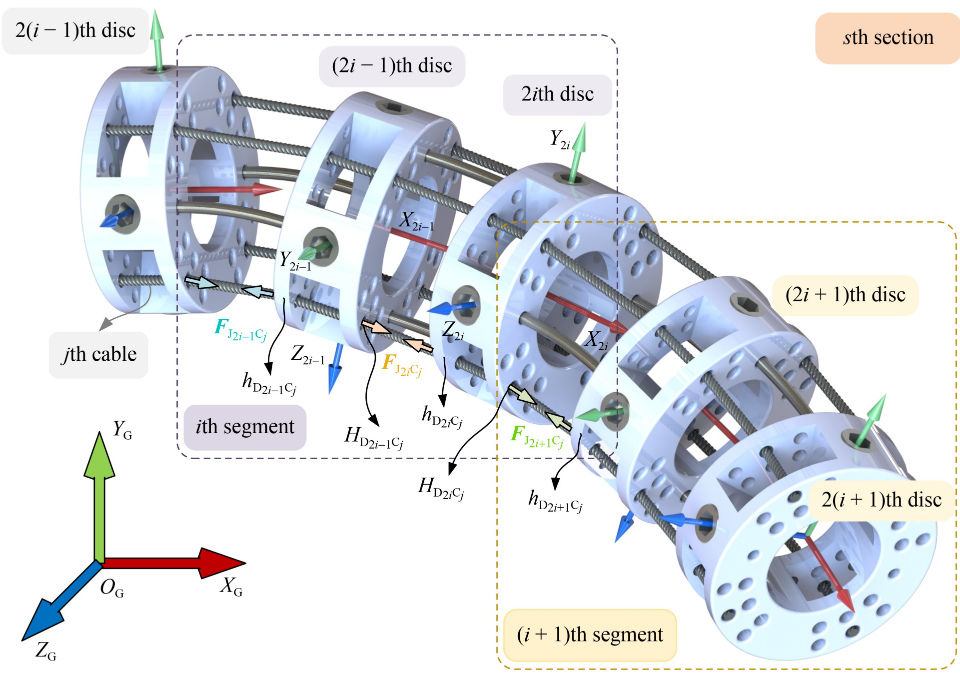

Fig. 5 Schematics of two-segment continuum robot.

$$\boldsymbol{F}^{O_{2i-1}}_{\mathrm{D}_{2i}\mathrm{C}_{j+2}} = \boldsymbol{F}^{O_{2i-1}}_{\mathrm{J}_{2i}\mathrm{C}_{j+2}} + \boldsymbol{F}^{O_{2i-1}}_{\mathrm{J}_{2i+1}\mathrm{C}_{j+2}} = F_{\mathrm{J}_{2i}\mathrm{C}_{j+2}} \cdot \frac{H^{O_{2i-1}}_{\mathrm{D}_{2i-1}\mathrm{C}_{j+2}} - h^{O_{2i-1}}_{\mathrm{D}_{2i}\mathrm{C}_{j+2}}}{\left\| H^{O_{2i-1}}_{\mathrm{D}_{2i-1}\mathrm{C}_{j+2}} - h^{O_{2i-1}}_{\mathrm{D}_{2i}\mathrm{C}_{j+2}} \right\|} + F_{\mathrm{J}_{2i+1}\mathrm{C}_{j+2}} \cdot \frac{h^{O_{2i-1}}_{\mathrm{D}_{2i+1}\mathrm{C}_{j+2}} - H^{O_{2i-1}}_{\mathrm{D}_{2i}\mathrm{C}_{j+2}}}{\left\| h^{O_{2i-1}}_{\mathrm{D}_{2i+1}\mathrm{C}_{j+2}} - H^{O_{2i-1}}_{\mathrm{D}_{2i}\mathrm{C}_{j+2}} \right\|}. \tag{6}$$

A particular case should be considered when the 2ith disc is the last disc of the sth section. Under this condition, the second item in Eq. (5) should be omitted (i.e., $\boldsymbol{F}^{O_{D_s-1}}_{\mathrm{D}_{D_s}\mathrm{C}_j} = \boldsymbol{F}^{O_{D_s-1}}_{\mathrm{J}_{D_s}\mathrm{C}_j}$). However, Eq. (5) can still apply to this case by assuming $F_{\mathrm{J}_{2i+1}\mathrm{C}_j}$ equals 0. In addition, the moment of actuating force relative to point O_{2i-1} expressed in frame $\{O_{2i-1}\}$ can be obtained by vector cross product

$$\boldsymbol{M}^{O_{2i-1}}_{\mathrm{D}_{2i}\mathrm{C}_j} = \left(h^{O_{2i-1}}_{\mathrm{D}_{2i}\mathrm{C}_j} - O^{O_{2i-1}}_{2i-1}\right) \times \boldsymbol{F}^{O_{2i-1}}_{\mathrm{J}_{2i}\mathrm{C}_j} + \left(H^{O_{2i-1}}_{\mathrm{D}_{2i}\mathrm{C}_j} - O^{O_{2i-1}}_{2i-1}\right) \times \boldsymbol{F}^{O_{2i-1}}_{\mathrm{J}_{2i+1}\mathrm{C}_j}, \tag{7}$$

where the lumped moment of actuating moments $\boldsymbol{M}^{O_{2i-1}}_{\mathrm{D}_{2i}\mathrm{C}_j}$ relative to point O_{2i-1} expressed in frame $\{O_{2i-1}\}$, and $O_i^{O_p}$ is point O_i expressed in frame $\{O_p\}$. They can be further described as follows:

$$\begin{cases} \boldsymbol{F}^{O_{2i-1}}_{\mathrm{D}_{2i}\mathrm{C}} = \displaystyle\sum_{j=4s-3}^{4K} \boldsymbol{F}^{O_{2i-1}}_{\mathrm{D}_{2i}\mathrm{C}_j}, \\ \boldsymbol{M}^{O_{2i-1}}_{\mathrm{D}_{2i}\mathrm{C}} = \displaystyle\sum_{j=4s-3}^{4K} \boldsymbol{M}^{O_{2i-1}}_{\mathrm{D}_{2i}\mathrm{C}_j}, \end{cases} \tag{8}$$

where $\boldsymbol{F}^{O_{2i-1}}_{\mathrm{D}_{2i}\mathrm{C}}$ and $\boldsymbol{M}^{O_{2i-1}}_{\mathrm{D}_{2i}\mathrm{C}}$ are the lumped force of actuating forces $\boldsymbol{F}^{O_{2i-1}}_{\mathrm{D}_{2i}\mathrm{C}_j}$ applied to the 2ith disc and K is the total number of sections.

Similarly, $\boldsymbol{F}^{O_{2(i-1)}}_{\mathrm{D}_{2i-1}\mathrm{C}_j}$ and $\boldsymbol{M}^{O_{2(i-1)}}_{\mathrm{D}_{2i-1}\mathrm{C}_j}$ can be easily obtained as

$$\begin{aligned} \boldsymbol{F}^{O_{2(i-1)}}_{\mathrm{D}_{2i-1}\mathrm{C}_j} &= \boldsymbol{F}^{O_{2(i-1)}}_{\mathrm{J}_{2i-1}\mathrm{C}_j} + \boldsymbol{F}^{O_{2(i-1)}}_{\mathrm{J}_{2i}\mathrm{C}_j} \\ &= F_{\mathrm{J}_{2i-1}\mathrm{C}_j} \cdot \frac{H^{O_{2(i-1)}}_{\mathrm{D}_{2(i-1)}\mathrm{C}_j} - h^{O_{2(i-1)}}_{\mathrm{D}_{2i-1}\mathrm{C}_j}}{\left\| H^{O_{2(i-1)}}_{\mathrm{D}_{2(i-1)}\mathrm{C}_j} - h^{O_{2(i-1)}}_{\mathrm{D}_{2i-1}\mathrm{C}_j} \right\|} + F_{\mathrm{J}_{2i}\mathrm{C}_j} \cdot \frac{h^{O_{2(i-1)}}_{\mathrm{D}_{2i}\mathrm{C}_j} - H^{O_{2(i-1)}}_{\mathrm{D}_{2i-1}\mathrm{C}_j}}{\left\| h^{O_{2(i-1)}}_{\mathrm{D}_{2i}\mathrm{C}_j} - H^{O_{2(i-1)}}_{\mathrm{D}_{2i-1}\mathrm{C}_j} \right\|}, \end{aligned} \tag{9}$$

$$\boldsymbol{M}^{O_{2(i-1)}}_{\mathrm{D}_{2i-1}\mathrm{C}_j} = \left(h^{O_{2(i-1)}}_{\mathrm{D}_{2i-1}\mathrm{C}_j} - O^{O_{2(i-1)}}_{2(i-1)}\right) \times \boldsymbol{F}^{O_{2(i-1)}}_{\mathrm{J}_{2i-1}\mathrm{C}_j} + \left(H^{O_{2(i-1)}}_{\mathrm{D}_{2i-1}\mathrm{C}_j} - O^{O_{2(i-1)}}_{2(i-1)}\right) \times \boldsymbol{F}^{O_{2(i-1)}}_{\mathrm{J}_{2i}\mathrm{C}_j}. \tag{10}$$

4.2 Cable-hole friction modeling

Friction has proven vital to improving the kinetostatic modeling accuracy of CDCRs [1,15]. In this paper, the friction between the driving cables and disc holes is studied based on the Coulomb friction model.

4.2.1 Variable friction coefficient formulation

According to the theoretical analysis in Section 2, the friction force on different sides of the disc can be modeled separately. Inspired by the friction test reported in Ref. [1], the variable friction coefficient model of the optimized configuration (Fig. 3) can be given by

$$\begin{cases} \mu_{2i,1} = f(\theta_{i,2}) = a\theta_{i,2}^2 + b\theta_{i,2} + c, \\ \mu_{2i,2} = f(\theta_{i+1,1}) = a\theta_{i+1,1}^2 + b\theta_{i+1,1} + c, \end{cases} \tag{11}$$

where $\mu_{2i,1}$ and $\mu_{2i,2}$ are the friction coefficients of the 2ith disc, which are experimentally identified in Section 4, $\theta_{i,2}$ and $\theta_{i+1,1}$ are the angles between the 2ith disc and cables, and they are half of the joint angles ($\beta_{i,2}$, $\beta_{i+1,1}$).

Thus, the frictional force $f_{\mathrm{D}_{2i}\mathrm{C}_j}$ at the 2ith disc along the jth cable can be calculated as

$$f_{\mathrm{D}_{2i}\mathrm{C}_j} = \mu_{2i,1}\left\|\boldsymbol{N}^{O_{2i}}_{\mathrm{D}_{2i}\mathrm{C}_j,1}\right\| + \mu_{2i,2}\left\|\boldsymbol{N}^{O_{2i}}_{\mathrm{D}_{2i}\mathrm{C}_j,2}\right\|, \tag{12}$$

where $\boldsymbol{N}^{O_{2i}}_{\mathrm{D}_{2i}\mathrm{C}_j,1}$ and $\boldsymbol{N}^{O_{2i}}_{\mathrm{D}_{2i}\mathrm{C}_j,2}$ are the pressure generated by the jth cable, which can be calculated as

$$\begin{cases} \boldsymbol{N}^{O_{2i}}_{\mathrm{D}_{2i}\mathrm{C}_j,1} = \boldsymbol{F}^{O_{2i}}_{\mathrm{J}_{2i}\mathrm{C}_j} - \boldsymbol{F}^{O_{2i}}_{\mathrm{J}_{2i}\mathrm{C}_j} \cdot \boldsymbol{n}^{O_{2i}}_{X_{2i}}, \\ \boldsymbol{N}^{O_{2i}}_{\mathrm{D}_{2i}\mathrm{C}_j,2} = \boldsymbol{F}^{O_{2i}}_{\mathrm{J}_{2i+1}\mathrm{C}_j} - \boldsymbol{F}^{O_{2i}}_{\mathrm{J}_{2i+1}\mathrm{C}_j} \cdot \boldsymbol{n}^{O_{2i}}_{X_{2i}}, \end{cases} \tag{13}$$

where $\boldsymbol{n}^{O_{2i}}_{X_{2i}}$ is the normal unit vector of the $Y_{2i}O_{2i}X_{2i}$ plane, expressed in frame $\{O_{2i}\}$.

4.2.2 Adaptive friction direction criterion

The last subsection provides the solution to calculate the value of the friction forces. However, the velocity is not involved in the kinematic model. Thus, the friction direction cannot be directly determined, and this topic is not investigated in the conventional static model. In this study, a novel methodology is proposed to determine the friction direction adaptively based on the kinematic parameters.

As illustrated in Fig. 5, $F_{\mathrm{J}_{2i}\mathrm{C}_j}$ and $F_{\mathrm{J}_{2i+1}\mathrm{C}_j}$ are the values of the jth cable tension of the $2i$th joint and the $(2i + 1)$th joint, respectively. The relationship between $F_{\mathrm{J}_{2i}\mathrm{C}_j}$ and $F_{\mathrm{J}_{2i+1}\mathrm{C}_j}$ can be given by

$$F_{\mathrm{J}_{2i+1}\mathrm{C}_j} = F_{\mathrm{J}_{2i}\mathrm{C}_j} + \mathrm{sgn}\left(\Delta L_{\mathrm{D}_{2i+1}\mathrm{C}_j}\right) \cdot f_{\mathrm{D}_{2i}\mathrm{C}_j}, \tag{14}$$

where $\Delta L_{\mathrm{D}_i\mathrm{C}_j}$ is the sum of the jth cable variation from the ith joint to the D_Kth joint, $\mathrm{sgn}\left(\Delta L_{\mathrm{D}_{2i+1}\mathrm{C}_j}\right)$ is employed to determine the friction direction. As illustrated in Fig. 6, the criterion of friction direction is proposed based on the analysis of kinematics parameters (i.e., $\Delta L_{\mathrm{D}_{2i+1}\mathrm{C}_j}$), which can be described as

$$\mathrm{sgn}\left(\Delta L_{\mathrm{D}_{2i+1}\mathrm{C}_j}\right) = \begin{cases} -1, \ \Delta L_{\mathrm{D}_{2i+1}\mathrm{C}_j} < 0, \\ 0, \ \Delta L_{\mathrm{D}_{2i+1}\mathrm{C}_j} = 0, \\ +1, \ \Delta L_{\mathrm{D}_{2i+1}\mathrm{C}_j} > 0. \end{cases} \tag{15}$$

Specifically, if $\Delta L_{\mathrm{D}_{2i+1}\mathrm{C}_j} < 0$, the motion direction of the jth cable is from the $(2i + 1)$th disc to the $2i$th disc. Thus, the friction direction on the jth cable along the direction of $+X_{2i}$, i.e., $\mathrm{sgn}\left(\Delta L_{\mathrm{D}_{2i+1}\mathrm{C}_j}\right) = -1$, $F_{\mathrm{J}_{2i+1}\mathrm{C}_j} = F_{\mathrm{J}_{2i}\mathrm{C}_j} - f_{\mathrm{D}_{2i}\mathrm{C}_j}$. Conversely, $\Delta L_{\mathrm{D}_{2i+1}\mathrm{C}_j} > 0$ indicates the friction direction along the $-X_{2i}$. Especially for $i = 0$, $F_{\mathrm{J}_0\mathrm{C}_j}$ and $f_{\mathrm{D}_0\mathrm{C}_j}$ present the initial actuating force and frictional force at the base disc (D_0 disc), respectively. The value of $F_{\mathrm{J}_0\mathrm{C}_j}$ can be measured by force sensors, i.e., $F_{\mathrm{J}_0\mathrm{C}_j} = F_{\mathrm{SC}_j}$, where F_{SC_j} is the value of the jth cable tension on the force sensor. Thus, $f_{\mathrm{D}_0\mathrm{C}_j}$ can be calculated by Eqs. (11)–(13). In addition, the value of $\Delta L_{\mathrm{D}_{2i+1}\mathrm{C}_j}$ can be obtained as

$$\Delta L_{\mathrm{D}_{2i+1}\mathrm{C}_j} = \sum_{m=2i+1}^{D_K} \Delta l_{\mathrm{D}_m\mathrm{C}_j}. \tag{16}$$

Up to now, the friction could be calculated by Eqs. (11)–(14). The friction direction could be determined by Eqs. (15) and (16). All cases of the friction direction on the ith segment are listed in Table 2.

4.3 Gravity modeling

As illustrated in Fig. 5, gravity is defined along the negative direction of the Y_G-axis of the world frame $\{O_\mathrm{G}\}$. In this part, the gravities of all components, consisting of discs, compliant backbones, cables, and cable-locking devices on the manipulator, are considered in kinetostatic modeling. The center-of-gravity shift of compliant backbones caused by deflection is also included. Thus, the gravity of the $(2i - 1)$th joint can be given by

$$\boldsymbol{G}^{O_\mathrm{G}}_{\mathrm{D}_{2i-1}} = [0 \quad -m_{\mathrm{D}_{2i-1}}g \quad 0 \quad 0]^\mathrm{T}, \tag{17}$$

$$\boldsymbol{G}^{O_\mathrm{G}}_{\mathrm{NiTi}_{2i-1}} = [0 \quad -m_{\mathrm{NiTi}_{2i-1}}g \quad 0 \quad 0]^\mathrm{T}, \tag{18}$$

$$\boldsymbol{G}^{O_\mathrm{G}}_{\mathrm{J}_{2i-1}\mathrm{C}_j} = [0 \quad -m_{\mathrm{J}_{2i-1}\mathrm{C}_j}g \quad 0 \quad 0]^\mathrm{T}, \tag{19}$$

$$\boldsymbol{G}^{O_\mathrm{G}}_{\mathrm{CLD}_{2i-1}\mathrm{C}_j} = [0 \quad -m_{\mathrm{CLD}_{2i-1}\mathrm{C}_j}g \quad 0 \quad 0]^\mathrm{T}, \tag{20}$$

where $m_{\mathrm{D}_{2i-1}}$, $m_{\mathrm{NiTi}_{2i-1}}$, $m_{\mathrm{J}_{2i-1}\mathrm{C}_j}$, and $m_{\mathrm{CLD}_{2i-1}\mathrm{C}_j}$ are the masses of the $(2i - 1)$th disc, the $(2i - 1)$th compliant backbone, the jth cable of the $(2i - 1)$th joint, and the jth cable-locking device on the $(2i - 1)$th disc, respectively. $\boldsymbol{G}^{O_\mathrm{G}}_{\mathrm{D}_{2i-1}}$, $\boldsymbol{G}^{O_\mathrm{G}}_{\mathrm{NiTi}_{2i-1}}$, $\boldsymbol{G}^{O_\mathrm{G}}_{\mathrm{J}_{2i-1}\mathrm{C}_j}$, $\boldsymbol{G}^{O_\mathrm{G}}_{\mathrm{CLD}_{2i-1}\mathrm{C}_j}$ are the gravity of them expressed in frame $\{O_\mathrm{G}\}$. The cables are arranged symmetrically on the disc,

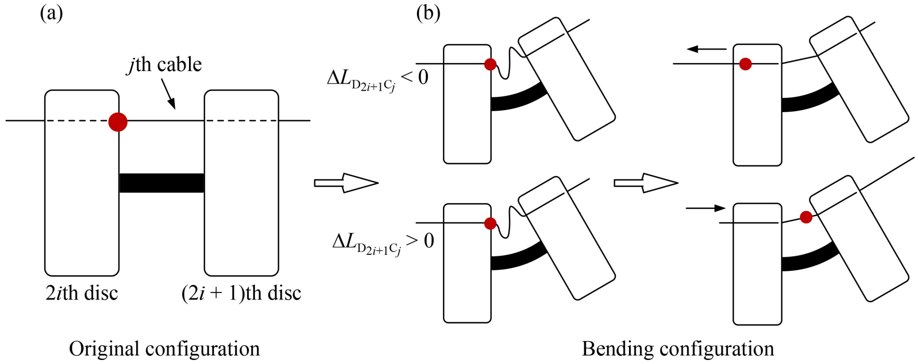

Fig. 6 Schematics of the criterion of friction direction.

Table 2 Cases of the *j*th cable actuating force of the *i*th segment

Case	Condition	Description
1	$\Delta L_{\mathrm{D}_{2i-1}\mathrm{C}_j} > 0, \Delta L_{\mathrm{D}_{2i}\mathrm{C}_j} > 0$	$F_{\mathrm{J}_{2i-1}\mathrm{C}_j} = F_{\mathrm{J}_{2(i-1)}\mathrm{C}_j} + f_{\mathrm{D}_{2(i-1)}\mathrm{C}_j}, F_{\mathrm{J}_{2i}\mathrm{C}_j} = F_{\mathrm{J}_{2i-1}\mathrm{C}_j} + f_{\mathrm{D}_{2i-1}\mathrm{C}_j}$
2	$\Delta L_{\mathrm{D}_{2i-1}\mathrm{C}_j} > 0, \Delta L_{\mathrm{D}_{2i}\mathrm{C}_j} = 0$	$F_{\mathrm{J}_{2i-1}\mathrm{C}_j} = F_{\mathrm{J}_{2(i-1)}\mathrm{C}_j} + f_{\mathrm{D}_{2(i-1)}\mathrm{C}_j}, F_{\mathrm{J}_{2i}\mathrm{C}_j} = F_{\mathrm{J}_{2i-1}\mathrm{C}_j}$
3	$\Delta L_{\mathrm{D}_{2i-1}\mathrm{C}_j} > 0, \Delta L_{\mathrm{D}_{2i}\mathrm{C}_j} < 0$	$F_{\mathrm{J}_{2i-1}\mathrm{C}_j} = F_{\mathrm{J}_{2(i-1)}\mathrm{C}_j} + f_{\mathrm{D}_{2(i-1)}\mathrm{C}_j}, F_{\mathrm{J}_{2i}\mathrm{C}_j} = F_{\mathrm{J}_{2i-1}\mathrm{C}_j} - f_{\mathrm{D}_{2i-1}\mathrm{C}_j}$
4	$\Delta L_{\mathrm{D}_{2i-1}\mathrm{C}_j} < 0, \Delta L_{\mathrm{D}_{2i}\mathrm{C}_j} > 0$	$F_{\mathrm{J}_{2i-1}\mathrm{C}_j} = F_{\mathrm{J}_{2(i-1)}\mathrm{C}_j} - f_{\mathrm{D}_{2(i-1)}\mathrm{C}_j}, F_{\mathrm{J}_{2i}\mathrm{C}_j} = F_{\mathrm{J}_{2i-1}\mathrm{C}_j} + f_{\mathrm{D}_{2i-1}\mathrm{C}_j}$
5	$\Delta L_{\mathrm{D}_{2i-1}\mathrm{C}_j} < 0, \Delta L_{\mathrm{D}_{2i}\mathrm{C}_j} = 0$	$F_{\mathrm{J}_{2i-1}\mathrm{C}_j} = F_{\mathrm{J}_{2(i-1)}\mathrm{C}_j} - f_{\mathrm{D}_{2(i-1)}\mathrm{C}_j}, F_{\mathrm{J}_{2i}\mathrm{C}_j} = F_{\mathrm{J}_{2i-1}\mathrm{C}_j}$
6	$\Delta L_{\mathrm{D}_{2i-1}\mathrm{C}_j} < 0, \Delta L_{\mathrm{D}_{2i}\mathrm{C}_j} < 0$	$F_{\mathrm{J}_{2i-1}\mathrm{C}_j} = F_{\mathrm{J}_{2(i-1)}\mathrm{C}_j} - f_{\mathrm{D}_{2(i-1)}\mathrm{C}_j}, F_{\mathrm{J}_{2i}\mathrm{C}_j} = F_{\mathrm{J}_{2i-1}\mathrm{C}_j} - f_{\mathrm{D}_{2i-1}\mathrm{C}_j}$
7	$\Delta L_{\mathrm{D}_{2i-1}\mathrm{C}_j} = 0, \Delta L_{\mathrm{D}_{2i}\mathrm{C}_j} > 0$	$F_{\mathrm{J}_{2i-1}\mathrm{C}_j} = F_{\mathrm{J}_{2(i-1)}\mathrm{C}_j}, F_{\mathrm{J}_{2i}\mathrm{C}_j} = F_{\mathrm{J}_{2i-1}\mathrm{C}_j} + f_{\mathrm{D}_{2i-1}\mathrm{C}_j}$
8	$\Delta L_{\mathrm{D}_{2i-1}\mathrm{C}_j} = 0, \Delta L_{\mathrm{D}_{2i}\mathrm{C}_j} = 0$	$F_{\mathrm{J}_{2i-1}\mathrm{C}_j} = F_{\mathrm{J}_{2(i-1)}\mathrm{C}_j}, F_{\mathrm{J}_{2i}\mathrm{C}_j} = F_{\mathrm{J}_{2i-1}\mathrm{C}_j}$
9	$\Delta L_{\mathrm{D}_{2i-1}\mathrm{C}_j} = 0, \Delta L_{\mathrm{D}_{2i}\mathrm{C}_j} < 0$	$F_{\mathrm{J}_{2i-1}\mathrm{C}_j} = F_{\mathrm{J}_{2(i-1)}\mathrm{C}_j}, F_{\mathrm{J}_{2i}\mathrm{C}_j} = F_{\mathrm{J}_{2i-1}\mathrm{C}_j} - f_{\mathrm{D}_{2i-1}\mathrm{C}_j}$

and the value of $m_{\mathrm{J}_{2i-1}\mathrm{C}_j}$ can be given by

$$m_{\mathrm{J}_{2i-1}\mathrm{C}_j} = \rho_{\mathrm{cable}} \cdot l_{\mathrm{D}_{2i-1}\mathrm{C}_j} = \rho_{\mathrm{cable}} \cdot \left(\Delta l_{\mathrm{D}_{2i-1}\mathrm{C}_j} + L\right), \tag{21}$$

where ρ_{cable} is the linear density of cable, $l_{\mathrm{D}_{2i-1}\mathrm{C}_j}$ is the *j*th cable length in *i*th segment. On the basis of the analysis of kinematics, Eqs. (17)–(20) can be further expressed in frame $\{O_{2i-2}\}$:

$$\boldsymbol{G}_{\mathrm{D}_{2i-1}}^{O_{2i-2}} = {}_{2i-2}^{\mathrm{G}}\boldsymbol{T}^{-1} \cdot \boldsymbol{G}_{\mathrm{D}_{2i-1}}^{O_{\mathrm{G}}}, \tag{22}$$

$$\boldsymbol{G}_{\mathrm{NiTi}_{2i-1}}^{O_{2i-2}} = {}_{2i-2}^{\mathrm{G}}\boldsymbol{T}^{-1} \cdot \boldsymbol{G}_{\mathrm{NiTi}_{2i-1}}^{O_{\mathrm{G}}}, \tag{23}$$

$$\boldsymbol{G}_{\mathrm{J}_{2i-1}\mathrm{C}_j}^{O_{2i-2}} = {}_{2i-2}^{\mathrm{G}}\boldsymbol{T}^{-1} \cdot \boldsymbol{G}_{\mathrm{J}_{2i-1}\mathrm{C}_j}^{O_{\mathrm{G}}}, \tag{24}$$

$$\boldsymbol{G}_{\mathrm{CLD}_{2i-1}\mathrm{C}_j}^{O_{2i-2}} = {}_{2i-2}^{\mathrm{G}}\boldsymbol{T}^{-1} \cdot \boldsymbol{G}_{\mathrm{CLD}_{2i-1}\mathrm{C}_j}^{O_{\mathrm{G}}}. \tag{25}$$

Correspondingly, the gravity-induced moment relative to point O_{2i-1} can be obtained in frame $\{O_{2i-2}\}$ as

$$\boldsymbol{M}_{\boldsymbol{G}_{\mathrm{D}_{2i-1}}}^{O_{2i-2}} = \left(O_{\mathrm{D}_{2i-1}}^{O_{2i-2}} - O_{2i-2}^{O_{2i-2}}\right) \times \boldsymbol{G}_{\mathrm{D}_{2i-1}}^{O_{2i-2}}, \tag{26}$$

$$\boldsymbol{M}_{\mathrm{NiTi}_{2i-1}}^{O_{2i-2}} = \left(O_{\mathrm{NiTi}_{2i-1}}^{O_{2i-2}} - O_{2i-2}^{O_{2i-2}}\right) \times \boldsymbol{G}_{\mathrm{NiTi}_{2i-1}}^{O_{2i-2}}, \tag{27}$$

$$\boldsymbol{M}_{\mathrm{J}_{2i-1}\mathrm{C}_j}^{O_{2i-2}} = \left(O_{\mathrm{J}_{2i-1}\mathrm{C}_j}^{O_{2i-2}} - O_{2i-2}^{O_{2i-2}}\right) \times \boldsymbol{G}_{\mathrm{J}_{2i-1}\mathrm{C}_j}^{O_{2i-2}}, \tag{28}$$

$$\boldsymbol{M}_{\mathrm{CLD}_{2i-1}\mathrm{C}_j}^{O_{2i-2}} = \left(O_{\mathrm{CLD}_{2i-1}\mathrm{C}_j}^{O_{2i-2}} - O_{2i-2}^{O_{2i-2}}\right) \times \boldsymbol{G}_{\mathrm{CLD}_{2i-1}\mathrm{C}_j}^{O_{2i-2}}, \tag{29}$$

where $O_{\mathrm{D}_{2i-1}}^{O_{2i-2}}$, $O_{\mathrm{NiTi}_{2i-1}}^{O_{2i-2}}$, $O_{\mathrm{J}_{2i-1}\mathrm{C}_j}^{O_{2i-2}}$, and $O_{\mathrm{CLD}_{2i-1}\mathrm{C}_j}^{O_{2i-2}}$ are the gravity center of the $(2i-1)$th disc, the $(2i-1)$th compliant backbone, the *j*th cable of the $(2i-1)$th joint, and *j*th cable-locking device on the $(2i-1)$th disc, respectively expressed in frame $\{O_{2i-2}\}$. $\boldsymbol{M}_{\boldsymbol{G}_{\mathrm{D}_{2i-1}}}^{O_{2i-2}}$, $\boldsymbol{M}_{\mathrm{NiTi}_{2i-1}}^{O_{2i-2}}$, $\boldsymbol{M}_{\mathrm{J}_{2i-1}\mathrm{C}_j}^{O_{2i-2}}$, $\boldsymbol{M}_{\mathrm{CLD}_{2i-1}\mathrm{C}_j}^{O_{2i-2}}$ are the moment of $\boldsymbol{G}_{\mathrm{D}_{2i-1}}^{O_{2i-2}}$, $\boldsymbol{G}_{\mathrm{NiTi}_{2i-1}}^{O_{2i-2}}$, $\boldsymbol{G}_{\mathrm{J}_{2i-1}\mathrm{C}_j}^{O_{2i-2}}$, and $\boldsymbol{G}_{\mathrm{CLD}_{2i-1}\mathrm{C}_j}^{O_{2i-2}}$ relative to point O_{2i-2} expressed in frame $\{O_{2i-2}\}$, respectively. The gravity center of the compliant backbone is slightly shifted as the deflection of the manipulator, which can be calculated as follows:

$$\cos\gamma_{i,1} = \frac{2}{\beta_{i,1}} \cdot \sin\frac{\beta_{i,1}}{2}, \tag{30}$$

where $\gamma_{i,1}$ represents the degree of the deviation of the center of the gravity of the Ni–Ti rod in the *i*th segment, as shown in Fig. 7. Hence, the position of $O_{\mathrm{NiTi}_{2i-1}}^{O_{2i-2}}$ expressed in frame $\{O_{2i-2}\}$ can be obtained easily. The position of $O_{\mathrm{J}_{2i-1}\mathrm{C}_j}^{O_{2i-2}}$ can be described as follows:

$$O_{\mathrm{J}_{2i-1}\mathrm{C}_j}^{O_{2i-2}} = \frac{1}{2} \cdot \left(H_{\mathrm{D}_{2i-2}\mathrm{C}_j}^{O_{2i-2}} + h_{\mathrm{D}_{2i-1}\mathrm{C}_j}^{O_{2i-2}}\right). \tag{31}$$

Similarly, the gravity analysis of the 2*i*th joint can be conducted without difficulty.

4.4 Backbone elasticity modeling

With the use of Kirchhoff elastic rod theory, each compliant backbone is assumed to be a constant arc. As illustrated in Figs. 3(c) and 7, the bending moment of the 2*i*th joint expressed in frame $\{O_{2i-1}\}$ can be formulated as follows:

$$\boldsymbol{M}_{\mathrm{J}_{2i}}^{O_{2i-1}} = \begin{bmatrix} 0 & 0 & \dfrac{2\beta_{i,2}}{L}EI_z & 0 \end{bmatrix}^{\mathrm{T}}, \tag{32}$$

where E is the Young's modulus, I_z is the moment of inertia of Ni–Ti rod, L is the length of Ni–Ti rod, which is inextensible, and $\boldsymbol{M}_{\mathrm{J}_i}^{O_{i-1}}$ is the bending moment of the *i*th joint expressed in frame $\{O_{i-1}\}$. Similarly, the bending of the $(2i-1)$th joint can be given by

$$\boldsymbol{M}_{\mathrm{J}_{2i-1}}^{O_{2(i-1)}} = \begin{bmatrix} 0 & 0 & \dfrac{2\beta_{i,1}}{L}EI_z & 0 \end{bmatrix}^{\mathrm{T}}. \tag{33}$$

4.5 External force and moment modeling

The interaction between the continuum robot and the environment is inevitable in the operation process, especially in confined- and narrow-space work. In addition, the end effector and some sensors are generally integrated into the continuum robot to perform various types of operations and perceive the configuration of the manipulator, resulting in external forces and moments applied to the continuum robot. Thus, these forces and moments are further considered in this study, which can be formulated as follows:

$$\boldsymbol{F}_{\mathrm{EX}_{2i}}^{O_{2i-1}} = {}_{2i-1}^{\mathrm{G}}\boldsymbol{T}^{-1} \cdot \boldsymbol{F}_{\mathrm{EX}_{2i}}^{O_{\mathrm{G}}}, \tag{34}$$

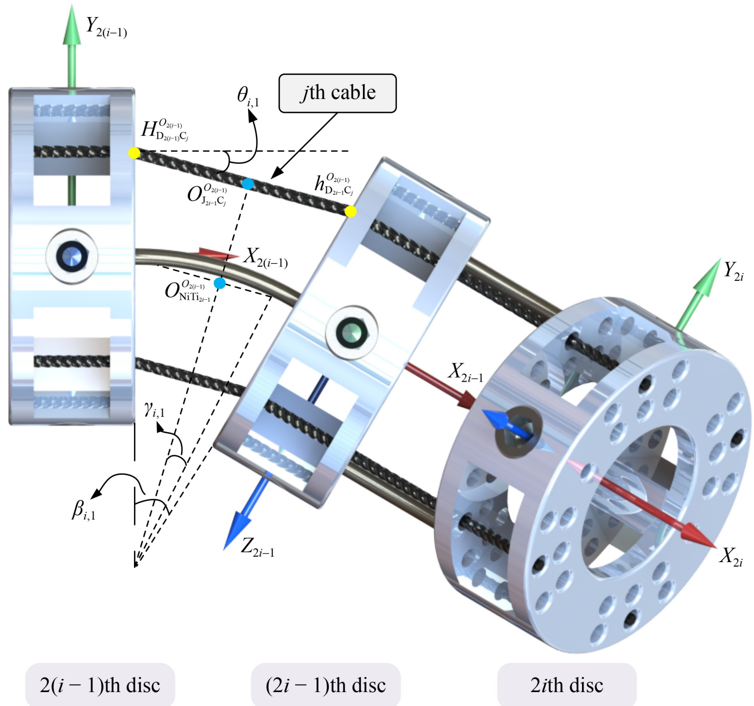

Fig. 7 Schematics of the gravity center of the compliant backbone.

$$\boldsymbol{M}^{O_{2i-1}}_{\mathrm{EX}_{2i}} = {}^{\mathrm{G}}_{2i-1}\boldsymbol{T}^{-1} \cdot \boldsymbol{M}^{O_{\mathrm{G}}}_{\mathrm{EX}_{2i}}, \tag{35}$$

where $\boldsymbol{F}^{O_{\mathrm{G}}}_{\mathrm{EX}_{2i}}$ and $\boldsymbol{M}^{O_{\mathrm{G}}}_{\mathrm{EX}_{2i}}$ are the external force and moment applied to the $2i$th disc expressed in frame $\{O_{\mathrm{G}}\}$, respectively. The moment of external force $\boldsymbol{F}^{O_{\mathrm{G}}}_{\mathrm{EX}_{2i}}$ relative to O_{2i-1} can be calculated as

$$\boldsymbol{M}^{O_{2i-1}}_{\boldsymbol{F}_{\mathrm{EX}_{2i}}} = \left(O^{O_{2i-1}}_{2i} - O^{O_{2i-1}}_{2i-1}\right) \times \boldsymbol{F}^{O_{2i-1}}_{\mathrm{EX}_{2i}}, \tag{36}$$

where $\boldsymbol{M}^{O_{i-1}}_{\boldsymbol{F}_{\mathrm{EX}_i}}$ is the moment of the external force $\boldsymbol{F}^{O_{\mathrm{G}}}_{\mathrm{EX}_i}$ relative to point O_{i-1} expressed in frame $\{O_{i-1}\}$.

4.6 Solutions

The kinetostatic equilibrium of the $2i$th joint is established by utilizing the Newton–Euler formula, which is formulated as follows:

$$\begin{cases} \boldsymbol{F}^{O_{2i-1}}_{\mathrm{D}_{2i-1}} = \boldsymbol{F}^{O_{2i-1}}_{\mathrm{D}_{2i}\mathrm{C}} + \boldsymbol{G}^{O_{2i-1}}_{\mathrm{D}_{2i}} + \boldsymbol{G}^{O_{2i-1}}_{\mathrm{NiTi}_{2i}} \\ \qquad + \displaystyle\sum_{j=4s-3}^{4K} \left(\boldsymbol{G}^{O_{2i-1}}_{\mathrm{J}_{2i}\mathrm{C}_j} + \boldsymbol{G}^{O_{2i-1}}_{\mathrm{CLD}_{2i}\mathrm{C}_j}\right) + \boldsymbol{F}^{O_{2i-1}}_{\mathrm{EX}_{2i}} + \boldsymbol{F}^{O_{2i-1}}_{\mathrm{D}_{2i}}, \\ \boldsymbol{M}^{O_{2i-1}}_{\mathrm{D}_{2i-1}} = \boldsymbol{M}^{O_{2i-1}}_{\mathrm{D}_{2i}\mathrm{C}} + \boldsymbol{M}^{O_{2i-1}}_{\boldsymbol{G}_{\mathrm{D}_{2i}}} + \boldsymbol{M}^{O_{2i-1}}_{\mathrm{NiTi}_{2i}} + \displaystyle\sum_{j=4s-3}^{4K} \left(\boldsymbol{M}^{O_{2i-1}}_{\mathrm{J}_{2i}\mathrm{C}_j} + \boldsymbol{M}^{O_{2i-1}}_{\mathrm{CLD}_{2i}\mathrm{C}_j}\right) \\ \qquad + \boldsymbol{M}^{O_{2i-1}}_{\mathrm{EX}_{2i}} + \boldsymbol{M}^{O_{2i-1}}_{\boldsymbol{F}_{\mathrm{EX}_{2i}}} + \boldsymbol{M}^{O_{2i-1}}_{\mathrm{D}_{2i}} + \boldsymbol{M}^{O_{2i-1}}_{\boldsymbol{F}_{\mathrm{D}_{2i}}}, \end{cases} \tag{37}$$

where $\boldsymbol{F}^{O_{2i-1}}_{\mathrm{D}_{2i-1}}$ and $\boldsymbol{M}^{O_{2i-1}}_{\mathrm{D}_{2i-1}}$ are the lumped force and lumped moment, respectively, on the $(2i-1)$th disc, which are expressed in frame $\{O_{2i-1}\}$. $\boldsymbol{F}^{O_{2i-1}}_{\mathrm{D}_{2i}}$, $\boldsymbol{M}^{O_{2i-1}}_{\mathrm{D}_{2i}}$, and $\boldsymbol{M}^{O_{2i-1}}_{\boldsymbol{F}_{\mathrm{D}_{2i}}}$ can be calculated as

$$\boldsymbol{F}^{O_{2i-1}}_{\mathrm{D}_{2i}} = {}^{2i-1}_{2i}\boldsymbol{T} \cdot \boldsymbol{F}^{O_{2i}}_{\mathrm{D}_{2i}}, \tag{38}$$

$$\boldsymbol{M}^{O_{2i-1}}_{\mathrm{D}_{2i}} = {}^{2i-1}_{2i}\boldsymbol{T} \cdot \boldsymbol{M}^{O_{2i}}_{\mathrm{D}_{2i}}, \tag{39}$$

$$\boldsymbol{M}^{O_{2i-1}}_{\boldsymbol{F}_{\mathrm{D}_{2i}}} = \left(O^{O_{2i-1}}_{2i} - O^{O_{2i-1}}_{2i-1}\right) \times \boldsymbol{F}^{O_{2i-1}}_{\mathrm{D}_{2i}}, \tag{40}$$

where $\boldsymbol{M}^{O_{2i-1}}_{\boldsymbol{F}_{\mathrm{D}_{2i}}}$ is the moment of the lumped force $\boldsymbol{F}^{O_{2i-1}}_{\mathrm{D}_{2i}}$ relative to point O_{i-1} expressed in frame $\{O_{i-1}\}$. A particular case that should be noted is that the items of $\boldsymbol{F}^{O_{2i-1}}_{\mathrm{D}_{2i}}$, $\boldsymbol{M}^{O_{2i-1}}_{\mathrm{D}_{2i}}$, and $\boldsymbol{M}^{O_{2i-1}}_{\boldsymbol{F}_{\mathrm{D}_{2i}}}$ in Eq. (36) should be omitted when the $2i$th disc is the last disc of the continuum robot (i.e., $2i = D_K$). One can assume these items as **0** to ensure that Eq. (37) still applies to this particular condition. The kinetostatic equilibrium of the $(2i-1)$th joint can be obtained similarly.

$$\begin{cases} \boldsymbol{F}^{O_{2(i-1)}}_{\mathrm{D}_{2(i-1)}} = \boldsymbol{F}^{O_{2(i-1)}}_{\mathrm{D}_{2i-1}\mathrm{C}} + \boldsymbol{G}^{O_{2(i-1)}}_{\mathrm{D}_{2i-1}} + \boldsymbol{G}^{O_{2(i-1)}}_{\mathrm{NiTi}_{2i-1}} \\ \qquad + \displaystyle\sum_{j=4s-3}^{4K} \left(\boldsymbol{G}^{O_{2(i-1)}}_{\mathrm{J}_{2i-1}\mathrm{C}_j} + \boldsymbol{G}^{O_{2(i-1)}}_{\mathrm{CLD}_{2i-1}\mathrm{C}_j}\right) + \boldsymbol{F}^{O_{2(i-1)}}_{\mathrm{EX}_{2i-1}} + \boldsymbol{F}^{O_{2(i-1)}}_{\mathrm{D}_{2i-1}}, \\ \boldsymbol{M}^{O_{2(i-1)}}_{\mathrm{D}_{2(i-1)}} = \boldsymbol{M}^{O_{2(i-1)}}_{\mathrm{D}_{2i-1}\mathrm{C}} + \boldsymbol{M}^{O_{2(i-1)}}_{\boldsymbol{G}_{\mathrm{D}_{2i-1}}} + \boldsymbol{M}^{O_{2(i-1)}}_{\mathrm{NiTi}_{2i-1}} \\ \qquad + \displaystyle\sum_{j=4s-3}^{4K} \left(\boldsymbol{M}^{O_{2(i-1)}}_{\mathrm{J}_{2i-1}\mathrm{C}_j} + \boldsymbol{M}^{O_{2(i-1)}}_{\mathrm{CLD}_{2i-1}\mathrm{C}_j}\right) \\ \qquad + \boldsymbol{M}^{O_{2(i-1)}}_{\mathrm{EX}_{2i-1}} + \boldsymbol{M}^{O_{2(i-1)}}_{\boldsymbol{F}_{\mathrm{EX}_{2i-1}}} + \boldsymbol{M}^{O_{2(i-1)}}_{\mathrm{D}_{2i-1}} + \boldsymbol{M}^{O_{2(i-1)}}_{\boldsymbol{F}_{\mathrm{D}_{2i-1}}}. \end{cases} \tag{41}$$

Thus, the kinetostatic equilibrium formulations of the CDCR chained by identical segments can be described by Eqs. (31), (32), (36), and (40). However, the kinetostatic items, such as $\boldsymbol{F}^{O_{2i-1}}_{\mathrm{D}_{2i}}$ and $\boldsymbol{M}^{O_{2i-1}}_{\mathrm{D}_{2i}}$ are coupled with kinematics parameters. Furthermore, the kinetostatic equilibrium of the ith segment is coupled with the equilibrium of the nth segment ($n = 1, 2, ..., i-1$). As a result, the joint angles $\beta_{i,1}$ and $\beta_{i,2}$ cannot be solved individually. A total of D_K independent scalar equations are separated from vector equations because the torsion problem of the twin-pivot continuum robot is ignored.

The nonlinearity of the above equations makes it challenging to solve analytically. In this paper, the Levenberg–Marquardt algorithm is employed to solve the kinetostatic equilibrium formulations iteratively. A single-section continuum robot prototype with six discs and four driving cables is studied to test the proposed kinetostatic model on a standard X86 PC with a 3.1 GHz CPU, and the number of test samples is 200. The results suggest that the average number of iterations is 1.72 s, and the average number of calculations is 8. The algorithm of the proposed kinetostatic model is illustrated in Table 3.

5 Identification of kinetomatics parameters

In this section, an experiment is designed to deduce the variable friction model and determine the coefficient. As illustrated in Fig. 8, the experiment platform mainly consists of a fixed base, a force sensor, pulleys, and payloads. The driving cable passes through the routing hole of the disc that is attached to the fixed base, with one end attached to the force sensing unit and the other attached to the payloads (i.e., 303.5, 353.5, 403.5, and 503.5 g). The position of pulleys is carefully designed to achieved a required angle between the cable and the disc (i.e., θ = 1°, 3°, 5°, 7°, and 9°, θ is the cable-hole angle). Five groups of experiments are conducted at different bending angles by applying four different payloads to

Table 3 Algorithm of the proposed kinetostatic model

Algorithm: kinetostatic model of twin-pivot continuum robot

Input:

➢ geometrical and mechanical properties ($N, K, E, L, I_z, h, \rho_{\mathrm{cable}}, m_{\mathrm{D}}, m_{\mathrm{NiTi}}, m_{\mathrm{CLD}}, r, \phi$)

➢ kinetostatics parameters ($\boldsymbol{F}_{\mathrm{SC}}, \boldsymbol{F}_{\mathrm{EX}}, \boldsymbol{M}_{\mathrm{EX}}$) , $\boldsymbol{F}_{\mathrm{SC}}$ is the matrix of $\boldsymbol{F}_{\mathrm{SC}_j}$, $\boldsymbol{F}_{\mathrm{EX}}$ is the matrix of $\boldsymbol{F}^{O_{\mathrm{G}}}_{\mathrm{EX}_i}$, $\boldsymbol{M}_{\mathrm{EX}}$ is the matrix of $\boldsymbol{M}^{O_{\mathrm{G}}}_{\mathrm{EX}_i}$

Output:

➢ bending angles of the continuum robot $\boldsymbol{\beta}_{2N\times 1}$ is the matrix of $\beta_{i,1}$ and $\beta_{i,2}$

1. Initialize the **bending angles** ($\boldsymbol{\beta} = \mathbf{0}$)
2. **for** $i = N$ to 1 **do**
3. $\beta_{i,1} = \boldsymbol{\beta}(2i-1, 1)$, $\beta_{i,2} = \boldsymbol{\beta}(2i, 1)$
4. **for** $j = 1$ to $4K$ **do**
5. $\Delta l_{\mathrm{D}_{2i-1}\mathrm{C}_j}, \Delta l_{\mathrm{D}_{2i}\mathrm{C}_j}, \mu_{2i-1,1}, \mu_{2i-1,2}, \mu_{2i,1}, \mu_{2i,2}, \boldsymbol{G}^{O_{2i-2}}_{\mathrm{J}_{2i-1}\mathrm{C}_j}, \boldsymbol{G}^{O_{2i-1}}_{\mathrm{J}_{2i}\mathrm{C}_j}$ ← Eqs. (4), (11), (19), and (21)
    6. **end for**
    7. **end for**
8. **for** $i = N$ to 1 **do**
9. **for** $j = 1$ to $4K$ **do**
10. Calculate $\Delta L_{\mathrm{D}_{2i+1}\mathrm{C}_j}$ and establish the criterion of friction direction ← Eqs. (15) and (16)
11. $\boldsymbol{F}^{O_{2(i-1)}}_{\mathrm{D}_{2i-1}\mathrm{C}}, \boldsymbol{F}^{O_{2i-1}}_{\mathrm{D}_{2i}\mathrm{C}}, \boldsymbol{G}^{O_{2(i-1)}}_{\mathrm{D}_{2i-1}}, \boldsymbol{G}^{O_{2i-1}}_{\mathrm{D}_{2i}}, \boldsymbol{G}^{O_{2(i-1)}}_{\mathrm{NiTi}_{2i-1}}, \boldsymbol{G}^{O_{2i-1}}_{\mathrm{NiTi}_{2i}}, \boldsymbol{G}^{O_{2(i-1)}}_{\mathrm{CLD}_{2i-1}\mathrm{C}_j}, \boldsymbol{G}^{O_{2i-1}}_{\mathrm{CLD}_{2i}\mathrm{C}_j}, \boldsymbol{F}^{O_{2(i-1)}}_{\mathrm{EX}_{2i-1}}, \boldsymbol{F}^{O_{2i-1}}_{\mathrm{EX}_{2i}}$,
12. $\boldsymbol{M}^{O_{2(i-1)}}_{\mathrm{D}_{2i-1}\mathrm{C}}, \boldsymbol{M}^{O_{2(i-1)}}_{\boldsymbol{G}_{\mathrm{D}_{2i-1}}}, \boldsymbol{M}^{O_{2(i-1)}}_{\mathrm{NiTi}_{2i-1}}, \boldsymbol{M}^{O_{2(i-1)}}_{\mathrm{J}_{2i-1}\mathrm{C}_j}, \boldsymbol{M}^{O_{2(i-1)}}_{\mathrm{CLD}_{2i-1}\mathrm{C}_j}, \boldsymbol{M}^{O_{2(i-1)}}_{\mathrm{EX}_{2i-1}}, \boldsymbol{M}^{O_{2(i-1)}}_{\boldsymbol{F}_{\mathrm{EX}_{2i-1}}}$,
13. $\boldsymbol{M}^{O_{2i-1}}_{\mathrm{D}_{2i}\mathrm{C}}, \boldsymbol{M}^{O_{2i-1}}_{\boldsymbol{G}_{\mathrm{D}_{2i}}}, \boldsymbol{M}^{O_{2i-1}}_{\mathrm{NiTi}_{2i}}, \boldsymbol{M}^{O_{2i-1}}_{\mathrm{J}_{2i}\mathrm{C}_j}, \boldsymbol{M}^{O_{2i-1}}_{\mathrm{CLD}_{2i}\mathrm{C}_j}, \boldsymbol{M}^{O_{2i-1}}_{\mathrm{EX}_{2i}}, \boldsymbol{M}^{O_{2i-1}}_{\boldsymbol{F}_{\mathrm{EX}_{2i}}}$ ← Eqs. (1)–(36)
14. $\begin{cases} \boldsymbol{f}(2i-1) = \boldsymbol{M}^{O_{2(i-1)}}_{\mathrm{D}_{2(i-1)}} - \boldsymbol{M}^{O_{2(i-1)}}_{\mathrm{J}_{2i-1}} \\ \boldsymbol{f}(2i) = \boldsymbol{M}^{O_{2i-1}}_{\mathrm{D}_{2i-1}} - \boldsymbol{M}^{O_{2i-1}}_{\mathrm{J}_{2i}} \end{cases}$ ← Eqs. (32), (33), (37)–(41)
    15. **end for**
    16. **end for**
17. Solve the $\boldsymbol{f}(\boldsymbol{\beta})$ by using the Levenberg–Marquardt algorithm
18. **if** $\boldsymbol{f}(\boldsymbol{\beta}^*)^{\mathrm{T}} \times \boldsymbol{f}(\boldsymbol{\beta}^*) < 1.0\mathrm{e}{-9}$
19. $\boldsymbol{\beta} \leftarrow \boldsymbol{\beta}^*$, $\boldsymbol{\beta} = \boldsymbol{\beta}^*$
    20. **end if**
    21. **return** $\boldsymbol{\beta}$

experimentally identify the coefficients of the variable friction model listed in Eq. (11). The least squares method is used to estimate the coefficients, and the results are illustrated in Fig. 9. This figure shows that the relationship between the friction coefficient and angle matches well with the proposed variable friction model.

6 Experimental validation

In this section, three continuum robot prototypes are constructed and integrated into the experimental platform. A set of experiments are performed to verify the proposed kinetostatic model and the cable-hole friction model. Furthermore, the experimental platform of the aero-engine model with blade array is established, where the validity of *in-situ* inspection based on the CDCR is tested.

6.1 Experimental setup

The continuum robot system integrated to experimentally validate the proposed kinetostatic model, which consists of the continuum manipulator, linear guide rail, DC motor, battery, signal amplifier, PC, control board (STM32F407), ESC, force sensor, wire locker, pulleys, and vision system, as illustrated in Fig. 10. Then, the whole continuum robot system is controlled by the linear motion of driving cables to achieve various complex morphologies of the manipulator. Three prototypes of CDCR with different length-to-diameter ratios and DOFs are constructed to verify the validity of the proposed models and test the performance of the presented CDCR, as shown in Fig. 11. During testing, a vision system with a 1920 × 1080 pixels DK camera is employed to perceive and evaluate the morphology of the tested prototype. Through our mechanism design, the screw located in the center of the disc can be regarded as a marker, which is employed initially to lock the compliant backbone and can be detected by the vision system. In the calculation process, we keep the position result to two decimal places (i.e., 0.01 mm), which depends on the VisionMaster software. In addition, the Ni–Ti rods are maintained in an

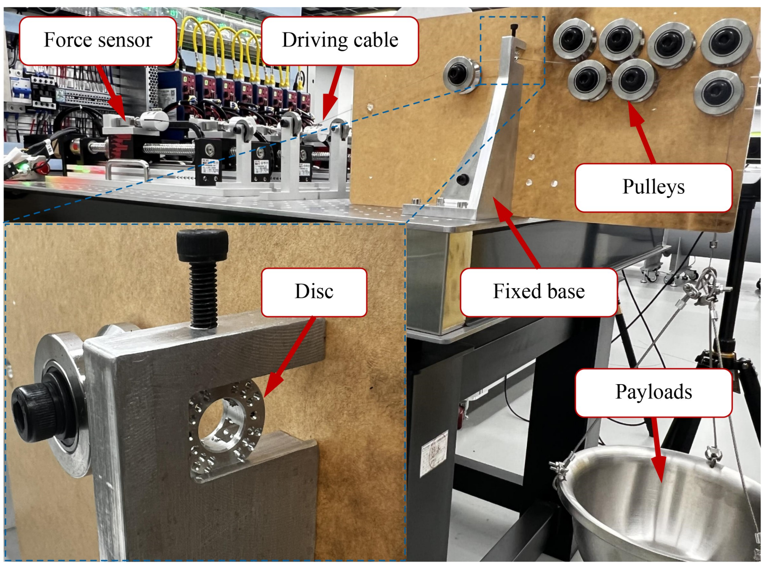

Fig. 8 Platform of friction coefficient.

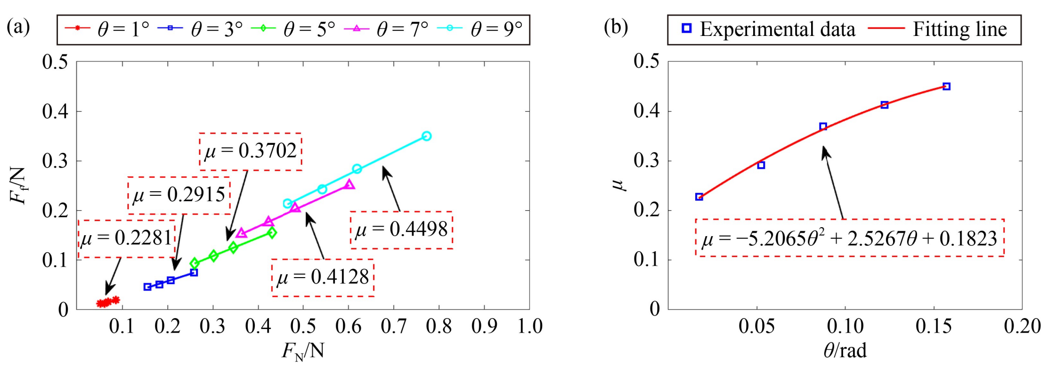

Fig. 9 Friction coefficient: (a) five groups of experimental results with different angles and (b) the relationship between friction coefficient and angle.

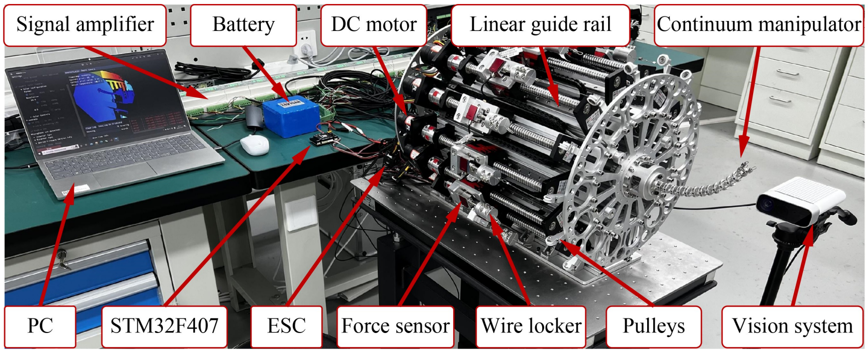

Fig. 10 Integrated continuum robot system. PC: personal computer, ESC: electronic speed controller.

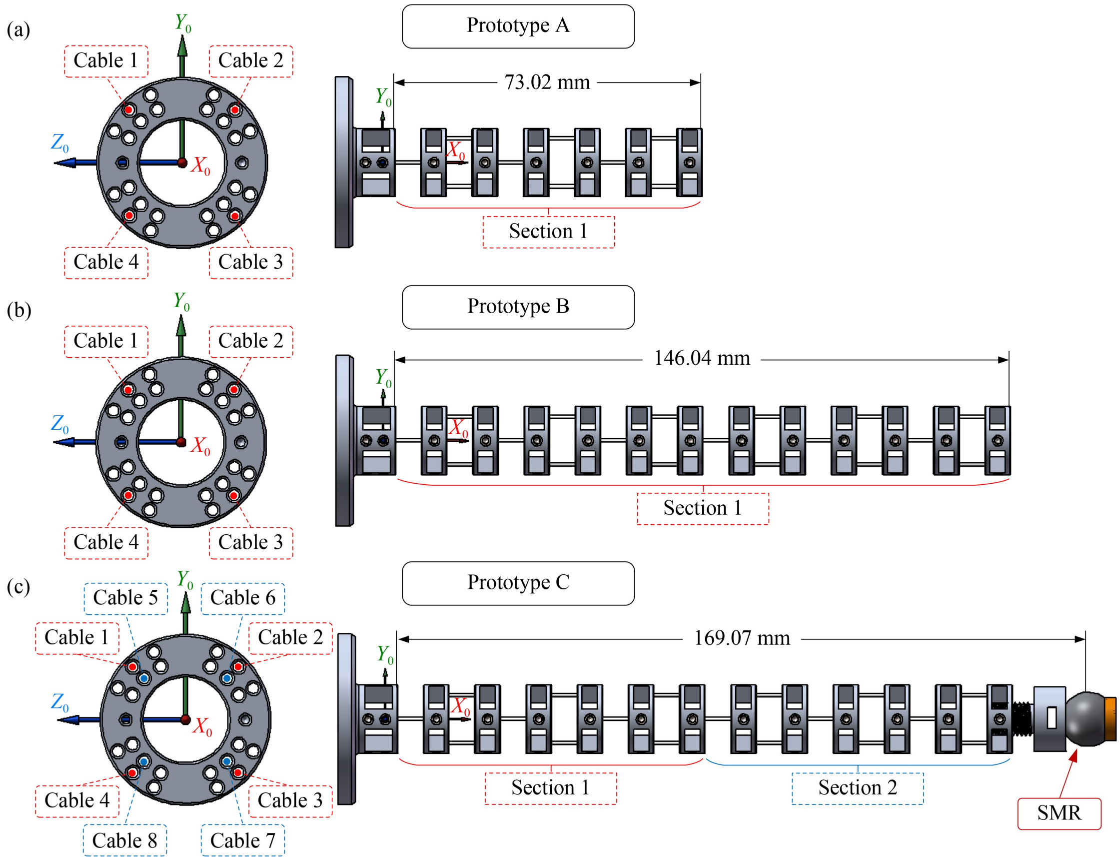

Fig. 11 Schematic of continuum robot prototypes. (a) Prototype A, (b) prototype B, and (c) prototype C.

elastic state during the experiments, and the maximum strain is less than 0.015. The Young's modulus of the Ni–Ti rod in this paper is 60.6 GPa. The force configurations of prototypes are listed in Table 4. Their modeling conditions are listed in Table 5 to enable the effects of friction, gravity, and payload to be studied better.

6.2 Experiments on single-section prototypes

In this section, four experiments are performed on two different length-to-diameter ratio prototypes to verify the effectiveness of the kinetostatic model by analyzing the effects of friction, gravity, and payload.

6.2.1 Effect of friction

On the basis of the experimental platform in Fig. 10, two groups of experiments listed in Table 4 are conducted to investigate the effects of friction on the proposed kinetostatic model. As illustrated in Fig. 12, the experimental, frictionless, and frictional results are represented by black circles, blue boxes, and red stars, respectively. As indicated in Fig. 12, the in-plane mean absolute errors

Table 4 Force configurations of prototypes

Case	Configurations			Case	Configurations		
	Prototype	Mass, $[m_1, m_2, m_3, m_4]$/kg	Payload/g		Prototype	Mass, $[m_1, m_2, m_3, m_4]$/kg	Payload/g
1	A	[1.03, 1.03, 0.06, 0.06]	0	16	B	[2.00, 2.00, 1.00, 1.00]	0
2	A	[0.90, 0.90, 0.10, 0.10]	0	17	B	[1.80, 1.80, 1.00, 1.00]	0
3	A	[0.74, 0.74, 0.13, 0.13]	0	18	B	[1.60, 1.60, 1.01, 1.01]	0
4	A	[0.68, 0.68, 0.24, 0.24]	0	19	B	[1.41, 1.41, 1.00, 1.00]	0
5	A	[0.60, 0.60, 0.34, 0.34]	0	20	B	[1.21, 1.21, 0.99, 0.99]	0
6	A	[0.55, 0.55, 0.50, 0.50]	0	21	B	[1.03, 1.03, 1.00, 1.00]	0
7	A	[0.42, 0.42, 0.56, 0.56]	0	22	B	[1.02, 1.02, 1.20, 1.20]	0
8	A	[0.29, 0.29, 0.62, 0.62]	0	23	B	[1.05, 1.05, 1.40, 1.40]	0
9	A	[0.20, 0.20, 0.70, 0.70]	0	24	B	[1.06, 1.06, 1.60, 1.60]	0
10	A	[0.12, 0.12, 0.80, 0.80]	0	25	B	[1.00, 1.00, 1.80, 1.80]	0
11	A	[0.06, 0.06, 0.92, 0.92]	0	26	B	[1.00, 1.00, 2.00, 2.00]	0
12	A	[1.06, 0.45, 0.12, 0.09]	0	27	B	[1.62, 1.35, 0.90, 1.00]	0
13	A	[0.45, 1.29, 0.13, 0.09]	0	28	B	[1.25, 1.50, 1.15, 0.85]	0
14	A	[0.12, 0.10, 1.06, 0.16]	0	29	B	[0.96, 1.05, 1.62, 1.41]	0
15	A	[0.13, 0.15, 0.24, 1.06]	0	30	B	[0.74, 1.04, 0.77, 1.72]	0
31	A	[0.28, 0.28, 0.50, 0.50]	20	37	B	[0.52, 0.52, 0.30, 0.30]	20
32	A	[0.38, 0.38, 0.40, 0.40]	20	38	B	[0.72, 0.72, 0.40, 0.40]	20
33	A	[0.62, 0.62, 0.40, 0.40]	20	39	B	[0.80, 0.80, 0.38, 0.38]	20
34	A	[1.11, 1.11, 0.67, 0.67]	20	40	B	[0.84, 0.84, 0.33, 0.33]	20
35	A	[1.40, 1.40, 0.75, 0.75]	20	41	B	[1.03, 1.03, 0.39, 0.39]	20
36	A	[1.21, 1.21, 0.38, 0.38]	20	42	B	[1.38, 1.38, 0.65, 0.65]	20

Table 5 Modeling conditions of the experiments on single-section prototype

Condition items	Constant friction	Variable friction	Disc gravity	Other-components gravities	Payload
Condition I	×	×	√	√	×
Condition II	×	√	√	√	×
Condition III	√	×	√	√	×
Condition IV	×	√	√	×	×
Condition V	×	√	√	√	√

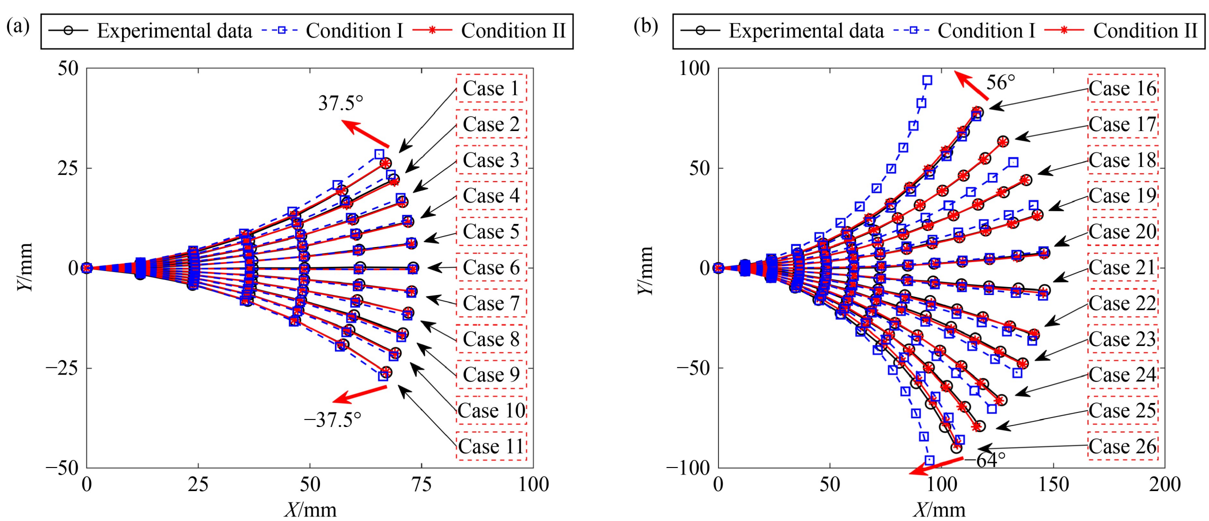

Fig. 12 Experimental results of friction effect: (a) tested on prototype A and (b) tested on prototype B.

(MAEs) of the tip position are 0.24 and 0.98 mm, which account for 0.33% and 0.67% of the entire length, respectively. The comparative results indicate that the proposed kinetostatic model can accurately predict the morphology of the continuum robot under different deflections.

However, once the friction is neglected, the position error will increase significantly as the deflection increases. The maximum error illustrated in Fig. 12(b) can reach more than 25 mm, thereby validating that cable-hole friction plays a significant role in precisely modeling the continuum robot. A comparison of the condition with/without friction (i.e., Conditions II and I) indicates that the proposed model outperforms the frictionless model in terms of position accuracy, with the tip position accuracy improving to a maximum of 89.69%. Another interesting phenomenon is that the friction effect will be reduced and may be neglected when the continuum robot is under a slight deflection or the manipulator length is small, indicating that a variable coefficient model is needed.

Another two groups of experiments are performed under a constant friction coefficient (i.e., μ = 0.3) to further demonstrate that the friction coefficient should be a function of joint angle rather than a constant value, and the results are shown in Fig. 13. The comparative results indicate that the kinetostatic model with a constant friction coefficient makes sense only under small deflection conditions but fails to accurately predict the morphology of the continuum robot under various large deflection conditions. Moreover, as the length of the manipulator increases, the in-plane MAE of the kinetostatic model with a constant friction coefficient increases, reaching 3.20 mm. Compared with the constant friction coefficient-based model, the proposed model characterizes the morphology very well under all deflection conditions and improves the modeling accuracy to 69.38%, thus verifying the validity of the proposed variable friction model.

6.2.2 Effect of gravity

In this part, an experiment is conducted to study the effects of other-component gravities (i.e., cables, compliant backbones, and cable-locking devices) on the manipulator. The results obtained by using the prototypes with different length-to-diameter ratios are illustrated in Fig. 14, where the CDCR morphology predicted by the proposed model that considers only the disc gravity and all-component gravities is marked with blue boxes and red stars, respectively. The comparative results in Fig. 14 suggest that the proposed kinetostatic model can well characterize the morphology of the prototypes with all-component gravities taken into consideration. A comparison of the results shown in Figs. 14(a) and 14(b) indicates that the effects of other-component gravities on position accuracy are non-negligible and will be enhanced as the length-to-diameter ratio increases. These effects may be neglected only when the length-to-ratio is very small. One may further note from Fig. 14(b) that the in-plane MAE of the CDCR tip position of condition IV is 7.25 mm, accounting for 4.96% of the entire length, while it is only 0.98 mm when the all-component gravities are considered. Therefore, the above gravity factors should be considered for accurate kinetostatic modeling, which improves the tip position accuracy to a maximum of 86.48%.

6.2.3 Effect of payload

External load tests are conducted by attaching a standard weight to the end of the continuum robot. Two groups of experiments are tested with a payload of 20 g, and the

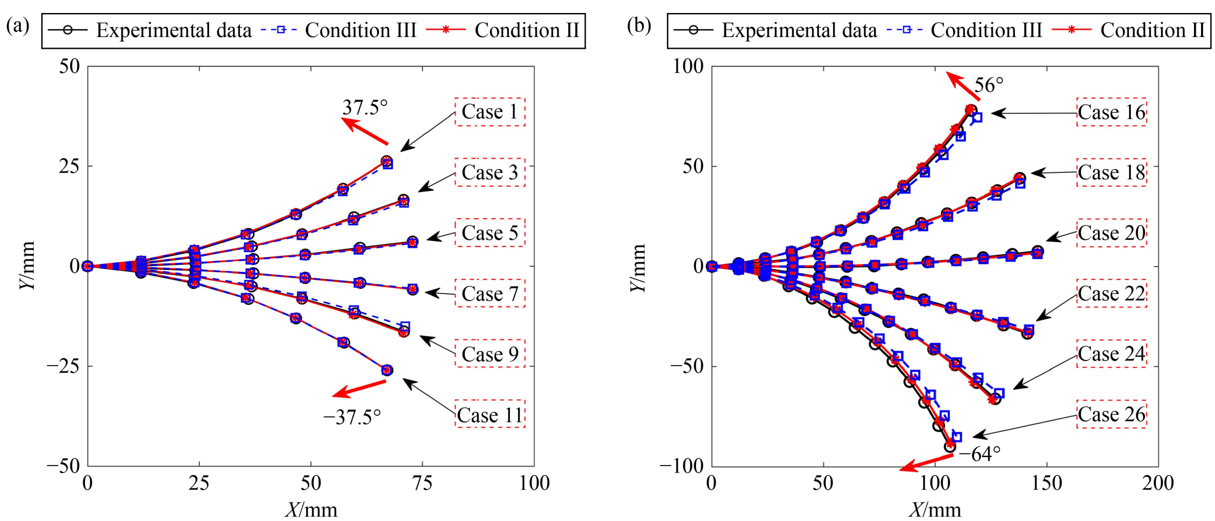

Fig. 13 Experimental results of constant/variable friction coefficient: (a) tested on prototype A and (b) tested on prototype B.

results are illustrated in Fig. 15. The masses of the two prototypes are 14.40 and 25.41 g, respectively. Figure 15 suggests that the in-plane MAEs of the tip position are 0.61 and 1.13 mm, accounting for only 0.84% and 0.77% of the entire length of the manipulator, respectively. The experimental results indicate that the morphology of the continuum robot predicted by the proposed model is in good agreement with the actual configuration, thus verifying the validity of the proposed model.

6.2.4 Effect of out-of-plane deflection

The above three experiments are designed to investigate the effects of friction, gravity, and payload in the plane, thus validating the effectiveness of the proposed model. In this subsection, an experiment is conducted to further analyze the morphology of CDCR with out-of-plane movement (three-dimensional), and the results are shown in Fig. 16. The out-of-plane MAEs of tip position are 2.41 and 6.73 mm, which account for 3.30% and 4.61% of the entire length, respectively. The out-of-plane position predicted by the proposed model may lead to larger (compared with in-plane position) but acceptable errors. These errors may be caused by torsional effects because they are not considered in the kinetostatic model.

6.3 Experiment on multi-section prototype

In this section, the trajectory tracking experiment is conducted on a multi-section prototype C to investigate the effect of continuous movement. The experimental platform of trajectory tracking is illustrated in Fig. 17. The tip position is continuously detected by a laser tracker at a frequency of 1000 Hz, and the mass of the spherically mounted retroreflector is 10 g. The actuating forces are collected by force sensors with a frequency of 5 Hz, which are illustrated in Fig. 18. The actuating forces of a pair of cables (such as F_1 and F_3, F_5 and F_7) show an opposite trend. The results of the tip trajectory are demonstrated in Fig. 19. According to the comparison results, the maximum trajectory error is within 9.30 mm, accounting for 5.50% of the entire length. The experimental results suggest that the proposed kinetostatic model

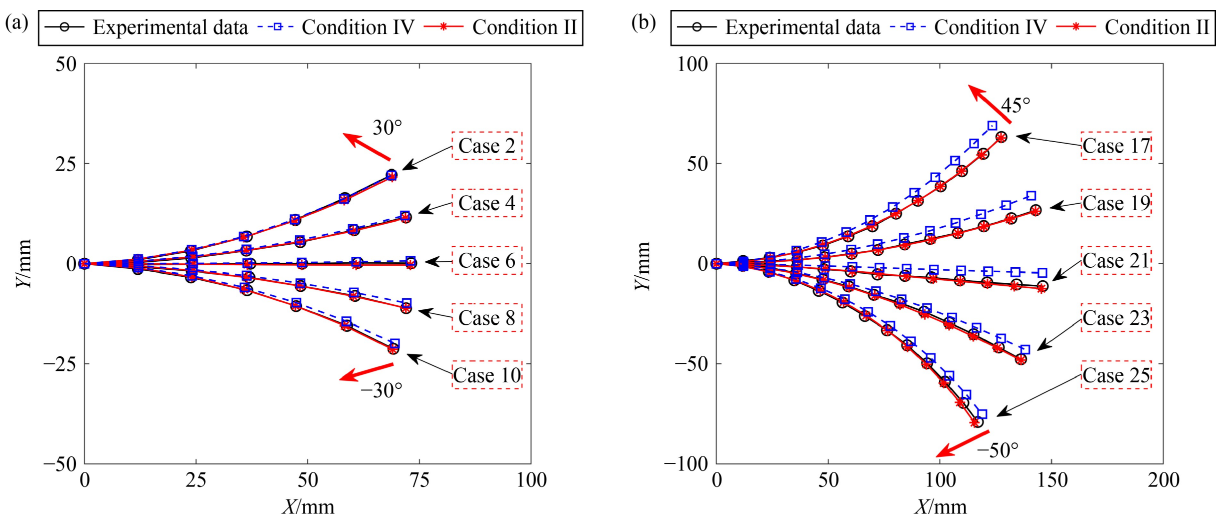

Fig. 14 Experimental results of gravity effect: (a) tested on prototype A and (b) tested on prototype B.

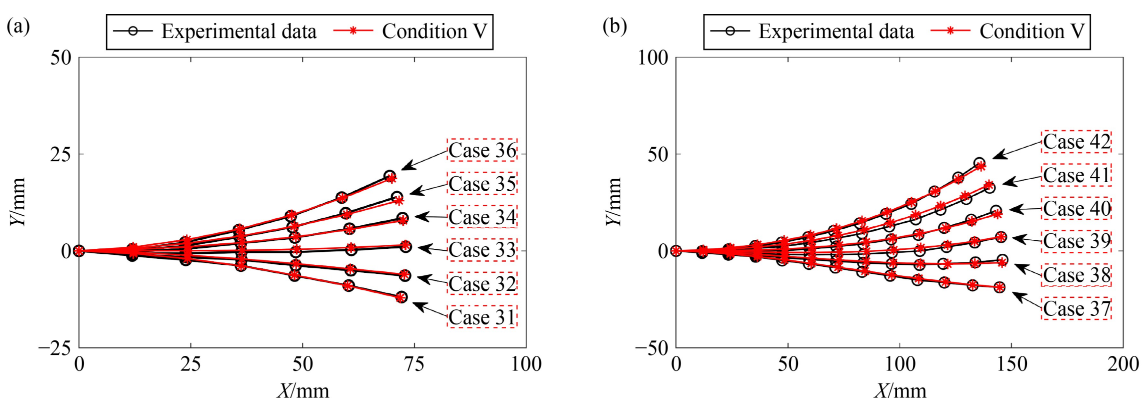

Fig. 15 Experimental results of payload effect: (a) tested on prototype A and (b) tested on prototype B.

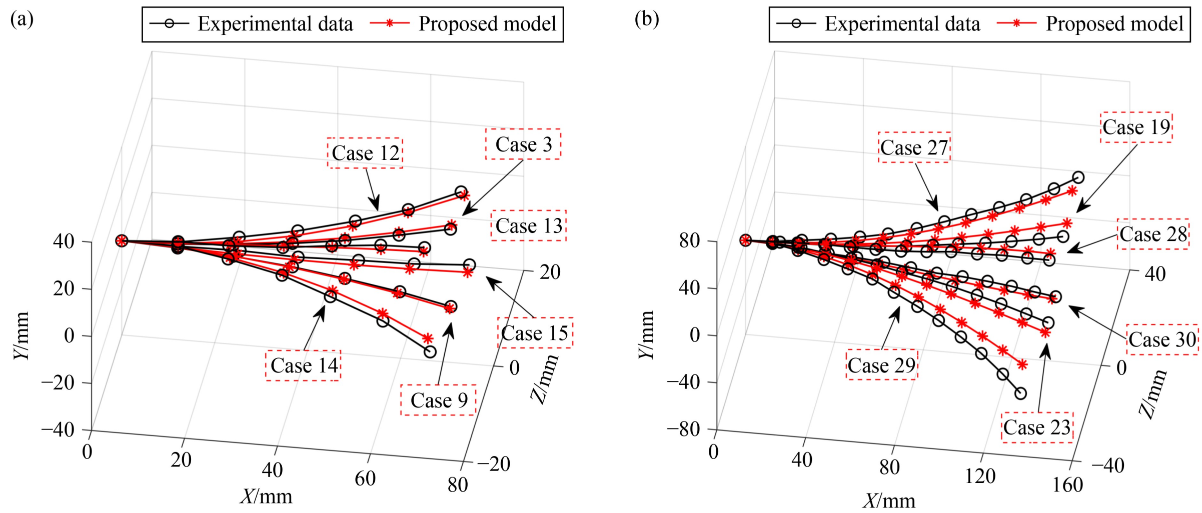

Fig. 16 Experimental results of out-of-plane deflection: (a) tested on prototype A and (b) tested on prototype B.

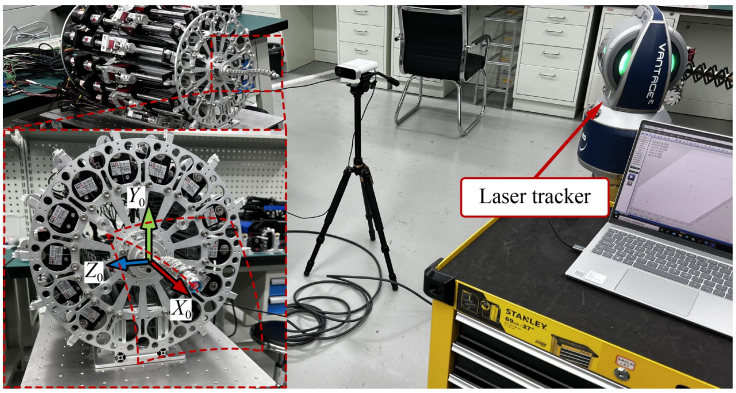

Fig. 17 Experiment of trajectory tracking.

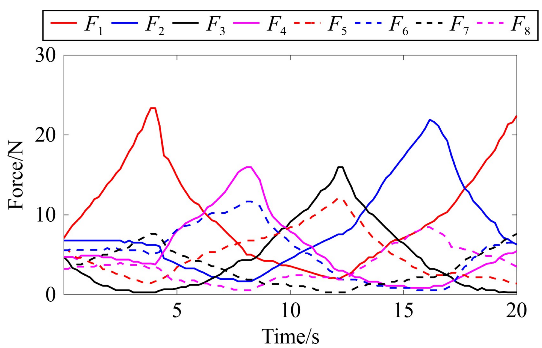

Fig. 18 Actuating forces of multi-section prototype.

can predict the tip position within an acceptable error when CDCR is continuously moving, thus establishing the foundation for the control of the continuum robot.

6.4 *In-situ* inspection experiment in aero-engines

A mock-up test rig is elaborately designed based on low-pressure compressor (LPC) blade arrays, as illustrated in Fig. 2, to further explore the possibility of applying CDCRs to perform *in-situ* maintenance tasks for aero-engines. The prototype of the CDCR shown in Fig. 3 is utilized to move across the unstructured and restricted space to perform the maintenance (inspection in this study) task. An end effector, i.e., an endoscope, is attached to the tip of the continuum manipulator, and another endoscope is employed to perceive the morphology of the CDCR when it moves across the blade arrays. In this case, a special path is designed for the CDCR to reach the second stage of LPC. According to the planned path, the follow-up movement of the CDCR is implemented, as shown in Fig. 20. The constructed CDCR successfully accesses the front of the engine (i.e., air intake) to the second stage of the LPC. This navigation experiment was conducted repeatedly to validate the robustness of the method in achieving the goal inspection task.

6.5 Discussion

The results of all five experimental tests demonstrate that the friction coefficient of the cable-hole friction model

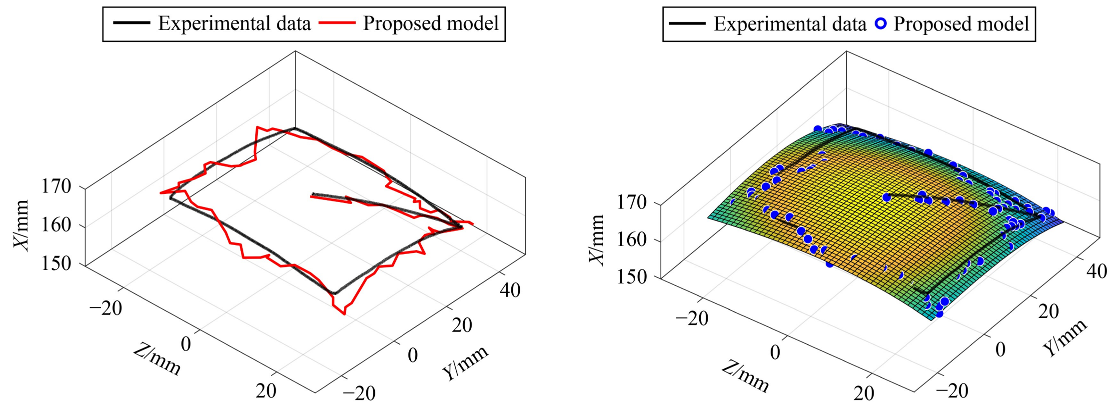

Fig. 19 Experimental results: (a) results of trajectory tracking and (b) scatterplot.

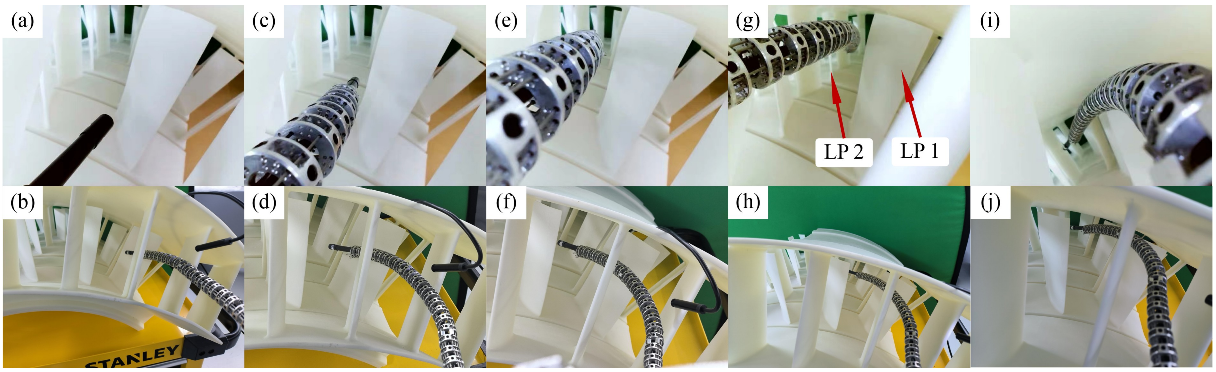

Fig. 20 Proposed continuum robot for *in-situ* inspection.

should be variable and can be expressed as a function of the joint angle. The analytical expression is deduced through theoretical analysis and structure optimization, whose parameters are identified through specially designed experiments. According to the analytical model of cable-hole friction coefficient, the friction coefficient increases with the increase in deflection. As a result of the nonlinearity of the cable-hole friction, the friction coefficient cannot be simply regarded as a constant value or a linear function of joint angle. Another phenomenon that should be noted from Fig. 12 is that when the continuum robot is under slight deflection, the effect of cable-hole friction is too tiny to be observed. This phenomenon is attributed to the little radial pressure under this condition, thereby leading to a small cable-hole friction force rather than the failure of the proposed cable-hole friction model.

With regard to another important issue, i.e., the gravity effect, in conventional static models, only the gravities of discs in CDCR are considered, and the influences of other components, including compliant backbones, cables, and cable-locking devices on the continuum manipulator, are always neglected. However, this paper found that these ignored factors may play a significant role in accurate modeling and morphology characterization. The theoretical and experimental results of this study demonstrate that the gravities have an almost monotonously linear effect on the position accuracy of the continuum robot. Thus, considering the gravity effects of all components will significantly benefit the high-fidelity kinetostatic modeling of CDCR.

The position errors bar of each disc of the CDCR prototypes for all designed experiments are presented in Fig. 21 to allow further analysis of the performance and advantages of the proposed kinetostatic model. Correspondingly, the average minimum and maximum tip position errors are listed in Table 6. The comparative results indicate that the proposed model outperforms other models that ignore the friction or gravity effects. The mean absolute percentage errors (MAPEs) for in-plane and out-of-plane movements are within 0.7% and 4.7%, respectively, which are acceptable for the control of CDCR.

These errors in this paper are mainly caused by manufacturing and assembly errors of the prototype, which are difficult to avoid. For example, for the assembly of the twin-pivot compliant mechanism, achieving an identical length between two compliant rods is difficult, thus resulting in geometric errors between the attached two discs. Ignoring these modeling uncertainties induced by manufacturing and assembly errors may cause the proposed kinetostatic model to be unable to

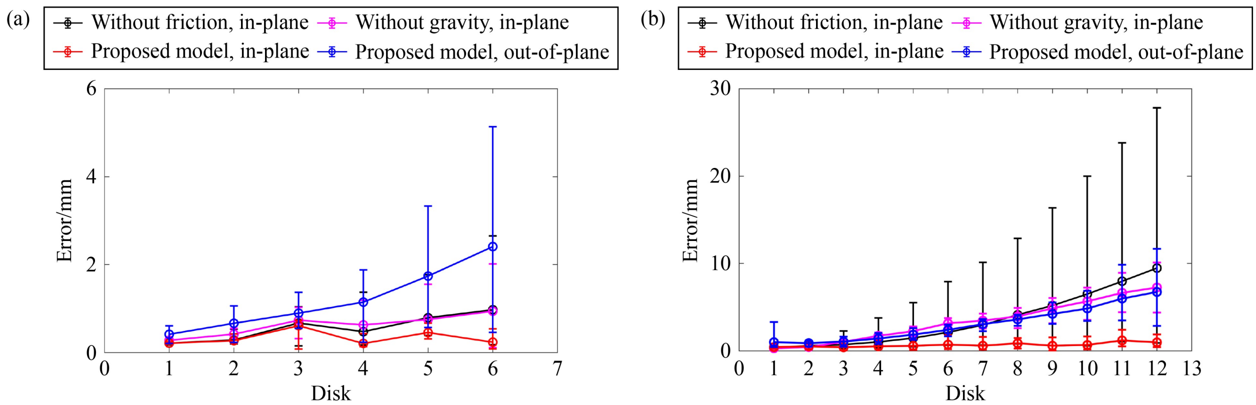

Fig. 21 Error bars of the continuum robot for different experiments: (a) tested on prototype A and (b) tested on prototype B.

Table 6 Tip position errors of the proposed model

Groups of tests	Tip position error/mm			Relative to the entire length/%		
	Average	Minimum	Maximum	Average	Minimum	Maximum
In-plane, prototype A	0.24	0.08	0.54	0.33	0.11	0.74
Out-of-plane, prototype A	2.41	0.46	5.14	3.30	0.63	7.04
In-plane, prototype B	0.98	0.42	1.89	0.67	0.29	1.29
Out-of-plane, prototype B	6.73	2.86	11.67	4.61	1.96	7.99

characterize the morphology of CDCRs precisely. In the future, these errors may be modeled as uncertainties and reduced through calibration. The difference between tip position errors of in-plane and out-of-plane movements may be attributed to the twisting issue and the cable-hole contact uncertainty, which are ignored in this study and will be considered in future work. Even though a previous study [6] demonstrated that the twisting effects of CDCR can be significantly reduced by the joint structure with a twin-pivot compliant mechanism, a small torsion phenomenon remains during out-of-plane movements. The cable-hole contact uncertainties caused by the gap between cable and hole include the variance of the cable-hole contact area and position. In this study, the effect of the cable-hole contact area was significantly reduced through structure optimization and novel cable-hole friction modeling. However, the cable-hole contact position variance that may occur in the moving process is ignored, especially when performing out-of-plane movements, which may contribute to the performance differences between in-plane and out-of-plane movements.

7 Conclusions

In this paper, a CDCR with a twin-pivot compliant mechanism is constructed and optimized for *in-situ* aero-engine maintenance, and a comprehensive kinetostatic model that considers the effects of cable-hole friction, gravity, and payload is proposed to characterize the morphology of the constructed CDCR. Specifically, a novel cable-hole friction model with the variable friction coefficient and adaptive friction direction criterion is developed to support the proposed kinetostatic model, and the gravity effects of all components are considered for the first time to deduce the proposed kinetostatic model. A set of experiments are elaborately designed and performed to verify the validity of the proposed model. The main conclusions can be summarized as follows:

1) First, the structure of the twin-pivot compliant mechanism is optimized, which makes it possible to model the cable-hole friction model on two sides of the disc separately and thus lays the foundation for cable-hole friction modeling. Through theoretical analysis and mathematical formulation, a novel cable-hole friction model is proposed based on the optimized twin-pivot compliant mechanism. The cable-hole friction coefficient on two sides of an arbitrary disc is separately modeled as a nonlinear function of joint angles on each side, and an adaptive friction direction determination criterion is presented based on the kinematics parameter analysis. The experimental results indicate that the proposed model has better position accuracy than the frictionless model and the model with a constant friction coefficient, improving more than 90% modeling accuracy.

2) Second, aside from the gravity effects of discs, the gravity effects of all other components, including the compliant backbones, cables, and cable-locking devices, are considered in the proposed kinetostatic model for the first time. The deflection-induced center-of-gravity shift of compliant joints is also involved in the proposed model. The experiment results indicate that the proposed

model improves the tip position accuracy to more than 80% compared with the model that does not consider the gravity effects of the components except for the discs. Therefore, the gravity effects of all components should be considered for accurate modeling if high accuracy is required.

3) Finally, 42 groups of experimental tests and the trajectory tracking experiment are conducted to verify the validity of the proposed kinetostatic model. The comparison results suggest that the in-plane and out-of-plane MAPEs are within 0.7% and 4.7%, respectively, demonstrating that the kinetostatic model successfully characterizes the morphology of the CDCR with an acceptable error. Furthermore, the validity of the kinetostatics lays the groundwork for intelligent control. In addition, the *in-situ* inspection experiment validates that the continuum robot can successfully reach the second stage of the LPC, thus establishing a foundation for performing *in-situ* maintenance tasks of aero-engines and other high-value-added equipment.

In addition, although the structure of twin-pivot compliant mechanism has effective torsion resistance, the torsion problem may also exist for a continuum robot that has a sizeable length-to-diameter ratio. Cable-hole position variance may occur during out-of-plane movements. Both effects of twisting and cable-hole contact uncertainty may contribute to tip position errors under large three-dimensional deflections. Effective solutions to address these issues may be considered in the future to improve the modeling accuracy further. In addition, we will further explore the application of the CDCR in aero-engines and other complex pipeline environments [38–40].

Nomenclature

Abbreviations

CDCR	Cable-driven continuum robot
D–H	Denavit–hartenberg
DC	Direct current
DOF	Degree of freedom
ESC	Electronic speed controller
FEM	Finite element method
LPC	Low-pressure compressor
MAE	Mean absolute error
MAPE	Mean absolute percentage error
PC	Personal computer
PCC	Piecewise constant curvature

Variables

C_i	Cable number
D_i	Disc number
E	Young's modulus of Ni–Ti rod
$f_{\mathrm{D}_i\mathrm{C}_j}$	Friction generated by the jth cable on the ith disc
$F_{\mathrm{J}_i\mathrm{C}_j}$	Value of the jth cable tension in the ith joint
F_{SC_j}	Value of the jth cable tension on the force sensor
$\boldsymbol{F}_{\mathrm{D}_i\mathrm{C}}^{O_{i-1}}$	Lumped force of actuating forces $\boldsymbol{F}_{\mathrm{D}_i\mathrm{C}_j}^{O_{i-1}}$ on the ith disc expressed in frame $\{O_{i-1}\}$
$\boldsymbol{F}_{\mathrm{D}_i\mathrm{C}_j}^{O_{i-1}}$	Actuating force vector applied by the jth cable to the ith disc expressed in frame $\{O_{i-1}\}$
$\boldsymbol{F}_{\mathrm{D}_i}^{O_{i-1}}$	Lumped forces on the ith disc expressed in frame $\{O_{i-1}\}$
$\boldsymbol{F}_{\mathrm{EX}}$	Matrix of $\boldsymbol{F}_{\mathrm{EX}_i}^{O_{\mathrm{G}}}$
$\boldsymbol{F}_{\mathrm{EX}_i}^{O_{\mathrm{G}}}$	External force applied to the ith disc expressed in frame $\{O_{\mathrm{G}}\}$
$\boldsymbol{F}_{\mathrm{J}_i\mathrm{C}_j}^{O_p}$	jth cable tension in the ith joint expressed in frame $\{O_p\}$
$\boldsymbol{F}_{\mathrm{SC}}$	Matrix of F_{SC_j}
$\boldsymbol{G}_{\mathrm{CLD}_i\mathrm{C}_j}^{O_{\mathrm{G}}}$	Gravity of the jth cable-locking device on the ith disc expressed in frame $\{O_{\mathrm{G}}\}$
$\boldsymbol{G}_{\mathrm{D}_i}^{O_{\mathrm{G}}}$	Gravity of the ith disc expressed in frame $\{O_{\mathrm{G}}\}$
$\boldsymbol{G}_{\mathrm{J}_i\mathrm{C}_j}^{O_{\mathrm{G}}}$	Gravity of the jth cable of the ith joint expressed in frame $\{O_{\mathrm{G}}\}$
$\boldsymbol{G}_{\mathrm{NiTi}_i}^{O_{\mathrm{G}}}$	Gravity of the Ni–Ti rod of the ith joint expressed in frame $\{O_{\mathrm{G}}\}$
g	Gravitational acceleration
h	Thickness of disc
$h_{\mathrm{D}_i\mathrm{C}_j}^{O_{\mathrm{G}}}$, $H_{\mathrm{D}_i\mathrm{C}_j}^{O_{\mathrm{G}}}$	jth cable holes on the ith disc
I_z	Moment of inertia of Ni–Ti rod
K	Number of sections
$l_{\mathrm{D}_{2i-1}\mathrm{C}_j}$, $l_{\mathrm{D}_{2i}\mathrm{C}_j}$	jth cable length in the ith segment
$\Delta l_{\mathrm{D}_{2i-1}\mathrm{C}_j}$, $\Delta l_{\mathrm{D}_{2i}\mathrm{C}_j}$	jth cable variations in the ith segment
L	Length of Ni–Ti rod
$\Delta L_{\mathrm{D}_i\mathrm{C}_j}$	Sum of the jth cable variation from the ith joint to the D_Kth joint
$m_{\mathrm{CLD}_i\mathrm{C}_j}$	Mass of the jth cable-locking device on the ith disc
m_{D_i}	Mass of the ith disc
$m_{\mathrm{J}_i\mathrm{C}_j}$	Mass of the jth cable of the ith joint
m_{NiTi_i}	Mass of the ith compliant backbone
$\boldsymbol{M}_{\mathrm{CLD}_i\mathrm{C}_j}^{O_{i-1}}$	Moment of the jth cable-locking device gravity $\boldsymbol{G}_{\mathrm{CLD}_i\mathrm{C}_j}$ relative to the point O_{i-1} expressed in frame $\{O_{i-1}\}$
$\boldsymbol{M}_{\mathrm{D}_i}^{O_{i-1}}$	Lumped moments relative to the point O_{i-1} expressed in frame $\{O_{i-1}\}$
$\boldsymbol{M}_{\mathrm{D}_i\mathrm{C}}^{O_{i-1}}$	Lumped moment of $\boldsymbol{M}_{\mathrm{D}_i\mathrm{C}_j}^{O_{i-1}}$ relative to point O_{i-1} expressed in frame $\{O_{i-1}\}$

$\boldsymbol{M}_{\mathrm{D}_i\mathrm{C}_j}^{O_{i-1}}$	Moment of actuating force $\boldsymbol{F}_{\mathrm{D}_i\mathrm{C}_j}^{O_{i-1}}$ relative to point O_{i-1} expressed in frame $\{O_{i-1}\}$
$\boldsymbol{M}_{\mathrm{EX}}$	Matrix of $\boldsymbol{M}_{\mathrm{EX}_i}^{O_\mathrm{G}}$
$\boldsymbol{M}_{\mathrm{EX}_i}^{O_\mathrm{G}}$	External moment applied to the ith disc expressed in frame $\{O_\mathrm{G}\}$
$\boldsymbol{M}_{\boldsymbol{F}_{\mathrm{D}_i}}^{O_{i-1}}$	Moment of the lumped force $\boldsymbol{F}_{\mathrm{D}_i}^{O_{i-1}}$ relative to point O_{i-1} expressed in frame $\{O_{i-1}\}$
$\boldsymbol{M}_{\boldsymbol{F}_{\mathrm{EX}_i}}^{O_{i-1}}$	Moment of the external force $\boldsymbol{F}_{\mathrm{EX}_i}^{O_\mathrm{G}}$ relative to point O_{i-1} expressed in frame $\{O_{i-1}\}$
$\boldsymbol{M}_{\boldsymbol{G}_{\mathrm{D}_i}}^{O_{i-1}}$	Moment of the ith disc gravity $\boldsymbol{G}_{\mathrm{D}_i}$ relative to the point O_{i-1} expressed in frame $\{O_{i-1}\}$
$\boldsymbol{M}_{\mathrm{J}_i\mathrm{C}_j}^{O_{i-1}}$	Moment of the jth cable gravity $\boldsymbol{G}_{\mathrm{J}_i\mathrm{C}_j}$ relative to the point O_{i-1} expressed in frame $\{O_{i-1}\}$
$\boldsymbol{M}_{\mathrm{J}_i}^{O_{i-1}}$	Bending moment of the ith joint expressed in frame $\{O_{i-1}\}$
$\boldsymbol{M}_{\mathrm{NiTi}_i}^{O_{i-1}}$	Moment of Ni–Ti rod gravity $\boldsymbol{G}_{\mathrm{NiTi}_i}$ relative to the point O_{i-1} expressed in frame $\{O_{i-1}\}$
N	Number of segments
$\boldsymbol{N}_{\mathrm{D}_i\mathrm{C}_j}^{O_i}$	Pressure generated by the jth cable on the ith disc expressed in frame $\{O_i\}$
$\boldsymbol{n}_{X_i}^{O_i}$	Normal unit vector of the $Y_iO_iX_i$ plane, expressed in frame $\{O_i\}$
$O_{\mathrm{CLD}_i\mathrm{C}_j}^{O_{i-1}}$	Gravity center of the jth cable-locking device on the ith disc, expressed in frame $\{O_{i-1}\}$
$O_{\mathrm{D}_i}^{O_{i-1}}$	Gravity center of the ith disc, expressed in frame $\{O_{i-1}\}$
$O_i^{O_p}$	Point O_i expressed in frame $\{O_p\}$
$O_{\mathrm{J}_i\mathrm{C}_j}^{O_{i-1}}$	Gravity center of the jth cable of the $(2i-1)$th joint, expressed in frame $\{O_{i-1}\}$
$O_{\mathrm{NiTi}_i}^{O_{i-1}}$	Gravity center of the ith compliant backbone, expressed in frame $\{O_{i-1}\}$
$\{o_{2i}\}: o-x_{2i}y_{2i}z_{2i}$	Revolute joint frame with origin o_{2i} at the axial intersection point of the $(2i-1)$th disc and the $2i$th disc
$\{O_\mathrm{G}\}: O-X_\mathrm{G}Y_\mathrm{G}Z_\mathrm{G}$	World frame and Y_G-axis is considered to be along the gravity direction
$\{O_i\}: O-X_iY_iZ_i$	ith disc frame with origin O_i at the center of the ith disc
r_j	Distance of the center of disc and the jth cable hole
$\mathbf{Rot}(x_i,\alpha)$	Rotation matrix (around the x_i-axis and the bending angle is α)
${}_{i+1}^{\ i}\boldsymbol{T}$	Homogeneous transformation matrix from $\{Q_i\}$ to $\{O_{i-1}\}$
$\mathbf{Trans}(x,y,z)$	Translation matrix
ρ_{cable}	Linear density of cables
$\beta_{i,1}, \beta_{i,2}$	Joint angles of the ith segment
$\boldsymbol{\beta}$	Results of the bending angle matrix
$\boldsymbol{\beta}^*$	Bending angle matrix during solving the kinetostatic equations
$\boldsymbol{\beta}_{2N\times1}$	Matrix of $\beta_{i,1}$ and $\beta_{i,2}$
ϕ_j	Angle of the jth cable hole and Y_i-axis
$\mu_{2i,1}, \mu_{2i,2}$	Friction coefficient of the $2i$th disc
θ	Cable-hole angle
$\theta_{i,1}, \theta_{i,2}$	Angel between the $2i$th disc and cables
$\gamma_{i,1}$	Degree of the deviation of the center of the gravity of the Ni–Ti rod in the ith segment

Acknowledgements This work was sponsored by the National Natural Science Foundation of China (Grant Nos. 52105117, 52375125, and 52105118).

Conflict of Interest The authors declare that they have no conflict of interest.

References

1. Wang M F, Dong X, Ba W M, Mohammad A, Axinte D, Norton A. Design, modelling and validation of a novel extra slender continuum robot for *in-situ* inspection and repair in aeroengine. Robotics and Computer-integrated Manufacturing, 2021, 67: 102054
2. Dong X, Axinte D, Palmer D, Cobos S, Raffles M, Rabani A, Kell J. Development of a slender continuum robotic system for on-wing inspection/repair of gas turbine engines. Robotics and Computer-integrated Manufacturing, 2017, 44: 218–229
3. Dong X, Wang M F, Mohammad A, Ba W M, Russo M, Norton A, Kell J, Axinte D. Continuum robots collaborate for safe manipulation of high-temperature flame to enable repairs in challenging environments. IEEE/ASME Transactions on Mechatronics, 2022, 27(5): 4217–4220
4. Russo M, Raimondi L, Dong X, Axinte D, Kell J. Task-oriented optimal dimensional synthesis of robotic manipulators with limited mobility. Robotics and Computer-integrated Manufacturing, 2021, 69: 102096
5. Dong X, Palmer D, Axinte D, Kell J. *In-situ* repair/maintenance

with a continuum robotic machine tool in confined space. Journal of Manufacturing Processes, 2019, 38: 313–318

6. Dong X, Raffles M, Cobos-Guzman S, Axinte D, Kell J. A novel continuum robot using twin-pivot compliant joints: design, modeling, and validation. Journal of Mechanisms and Robotics, 2016, 8(2): 021010
7. Dong X, Raffles M, Cobos Guzman S, Axinte D, Kell J. Design and analysis of a family of snake arm robots connected by compliant joints. Mechanism and Machine Theory, 2014, 77: 73–91
8. Li S Y, Hao G B. Current trends and prospects in compliant continuum robots: a survey. Actuators, 2021, 10(7): 145
9. Garriga-Casanovas A, Rodriguez Y Baena F. Kinematics of continuum robots with constant curvature bending and extension capabilities. Journal of Mechanisms and Robotics, 2019, 11(1): 011010
10. Webster R J III, Jones B A. Design and kinematic modeling of constant curvature continuum robots: a review. The International Journal of Robotics Research, 2010, 29(13): 1661–1683
11. Rao P, Peyron Q, Lilge S, Burgner-Kahrs J. How to model tendon-driven continuum robots and benchmark modelling performance. Frontiers in Robotics and AI, 2021, 7: 630245
12. Guo H, Ju F, Cao Y F, Qi F, Bai D M, Wang Y Y, Chen B. Continuum robot shape estimation using permanent magnets and magnetic sensors. Sensors and Actuators A: Physical, 2019, 285: 519–530
13. Yang Z S, Yang L H, Xu L, Chen X F, Guo Y J, Liu J X, Sun Y. A continuum robot with twin-pivot structure: the kinematics and shape estimation. In: Liu X J, Nie Z G, Yu J J, Xie F G, Song R, eds. Intelligent Robotics and Applications. Cham: Springer, 2021, 466–475
14. Chen X Q, Zhang X, Huang Y Y, Cao L, Liu J G. A review of soft manipulator research, applications, and opportunities. Journal of Field Robotics, 2022, 39(3): 281–311
15. Yuan H, Zhou L L, Xu W F. A comprehensive static model of cable-driven multi-section continuum robots considering friction effect. Mechanism and Machine Theory, 2019, 135: 130–149
16. Chen Y Y, Wu B B, Jin J B, Xu K. A variable curvature model for multi-backbone continuum robots to account for inter-segment coupling and external disturbance. IEEE Robotics and Automation Letters, 2021, 6(2): 1590–1597
17. Godage I S, Medrano-Cerda G A, Branson D T, Guglielmino E, Caldwell D G. Modal kinematics for multisection continuum arms. Bioinspiration & Biomimetics, 2015, 10(3): 035002
18. Yuan H, Chiu P W Y, Li Z. Shape-reconstruction-based force sensing method for continuum surgical robots with large deformation. IEEE Robotics and Automation Letters, 2017, 2(4): 1972–1979
19. Gonthina P S, Kapadia A D, Godage I S, Walker I D. Modeling variable curvature parallel continuum robots using euler curves. In: Proceedings of 2019 International Conference on Robotics and Automation. Montreal: IEEE, 2019, 1679–1685
20. Singh I, Amara Y, Melingui A, Mani Pathak P, Merzouki R. Modeling of continuum manipulators using pythagorean hodograph curves. Soft Robotics, 2018, 5(4): 425–442
21. Mbakop S, Tagne G, Drakunov S V, Merzouki R. Parametric PH curves model based kinematic control of the shape of mobile soft manipulators in unstructured environment. IEEE Transactions on Industrial Electronics, 2022, 69(10): 10292–10300
22. Huang X J, Zou J, Gu G Y. Kinematic modeling and control of variable curvature soft continuum robots. IEEE/ASME Transactions on Mechatronics, 2021, 26(6): 3175–3185
23. Dong X. Design of a continuum robot for *in-situ* repair of aero engine. Dissertation for the Doctoral Degree. Nottingham: University of Nottingham, 2016
24. Morales Bieze T, Kruszewski A, Carrez B, Duriez C. Design, implementation, and control of a deformable manipulator robot based on a compliant spine. The International Journal of Robotics Research, 2020, 39(14): 1604–1619
25. Li S J, Kruszewski A, Guerra T M, Nguyen A T. Equivalent-input-disturbance-based dynamic tracking control for soft robots via reduced-order finite-element models. IEEE/ASME Transactions on Mechatronics, 2022, 27(5): 4078–4089
26. Zhang J Y, Fang Q, Xiang P Y, Sun D Y, Xue Y N, Jin R, Qiu K, Xiong R, Wang Y, Lu H J. A survey on design, actuation, modeling, and control of continuum robot. Cyborg and Bionic Systems, 2022, 2022: 9754697
27. Janabi-Sharifi F, Jalali A, Walker I D. Cosserat rod-based dynamic modeling of tendon-driven continuum robots: a tutorial. IEEE Access: Practical Innovations, Open Solutions, 2021, 9: 68703–68719
28. Ghafoori M, Keymasi Khalaji A. Modeling and experimental analysis of a multi-rod parallel continuum robot using the cosserat theory. Robotics and Autonomous Systems, 2020, 134: 103650
29. Rucker D C, Jones B A, Webster R J III. A geometrically exact model for externally loaded concentric-tube continuum robots. IEEE Transactions on Robotics, 2010, 26(5): 769–780
30. Bretl T, McCarthy Z. Quasi-static manipulation of a kirchhoff elastic rod based on a geometric analysis of equilibrium configurations. The International Journal of Robotics Research, 2014, 33(1): 48–68
31. Awtar S, Sen S. A generalized constraint model for two-dimensional beam flexures: nonlinear strain energy formulation. Journal of Mechanical Design, 2010, 132(8): 081009
32. Chen G M, Ma F L, Hao G B, Zhu W D. Modeling large deflections of initially curved beams in compliant mechanisms using chained beam constraint model. Journal of Mechanisms and Robotics, 2019, 11(1): 011002
33. Ma F L, Chen G M. Kinetostatic modeling and characterization of compliant mechanisms containing flexible beams of variable effective length. Mechanism and Machine Theory, 2020, 147: 103770
34. Qi F, Ju F, Bai D M, Chen B. Kinematics optimization and static analysis of a modular continuum robot used for minimally invasive surgery. Proceedings of the Institution of Mechanical Engineers, Part H: Journal of Engineering in Medicine, 2018, 232(2): 135–148
35. Rucker D C, Webster R J III. Statics and dynamics of continuum robots with general tendon routing and external loading. IEEE Transactions on Robotics, 2011, 27(6): 1033–1044
36. Roy R, Wang L, Simaan N. Modeling and estimation of friction, extension, and coupling effects in multisegment continuum robots.

IEEE/ASME Transactions on Mechatronics, 2017, 22(2): 909–920
37. Mohammad A, Russo M, Fang Y H, Dong X, Axinte D, Kell J. An efficient follow-the-leader strategy for continuum robot navigation and coiling. IEEE Robotics and Automation Letters, 2021, 6(4): 7493–7500
38. Virgala I, Kelemen M, Božek P, Bobovský Z, Hagara M, Prada E, Oščádal P, Varga M. Investigation of snake robot locomotion possibilities in a pipe. Symmetry, 2020, 12(6): 939
39. Nikitin Y, Božek P, Peterka J. Logical-linguistic model of diagnostics of electric drives with sensors support. Sensors, 2020, 20(16): 4429
40. Abramov I V, Abramov A I, Nikitin Y R, Sosnovich E, Božek P, Stollmann V. Diagnostics of electrical drives. In: Proceedings of 2015 International Conference on Electrical Drives and Power Electronics. Tatranska Lomnica: IEEE, 2015, 364–367